AEDC-TR-79-49

Measurements in the Turbulent Boundary Layer at Constant Pressure in Subsonic and Supersonic Flow

Part II. Laser-Doppler Velocity Measurements

Paul E. Dimotakis, Donald J. Collins, and Daniel B. Lang
Jet Propulsion Laboratory
California Institute of Technology
Pasadena, California 91103

July 1979

Approved for public release; distribution unlimited.

ARNOLD ENGINEERING DEVELOPMENT CENTER
ARNOLD AIR FORCE STATION, TENNESSEE
AIR FORCE SYSTEMS COMMAND
UNITED STATES AIR FORCE

NOTICES

When U. S. Government drawings, specifications, or other data are used for any purpose other than a definitely related Government procurement operation, the Government thereby incurs no responsibility nor any obligation whatsoever, and the fact that the Government may have formulated, furnished, or in any way supplied the said drawings, specifications, or other data, is not to be regarded by implication or otherwise, or in any manner licensing the holder or any other person or corporation, or conveying any rights or permission to manufacture, use, or sell any patented invention that may in any way be related thereto.

Qualified users may obtain copies of this report from the Defense Documentation Center.

References to named commerical products in this report are not to be considered in any sense as an indorsement of the product by the United States Air Force or the Government.

This final report was submitted by Jet Propulsion Laboratory, California Institute of Technology, Pasadena, California 91103, under contracts F44620-75-C-0007, F44620-76-C-0046, MIPR EY 7483-76-0003, and EY 7483-76-0009, with the Arnold Engineering Development Center, Air Force Systems Command, Arnold Air Force Station, Tennessee 37389. Mr. Elton R. Thompson, AEDC/DOTR, was the Air Force project manager.

This report has been reviewed by the Information Office (OI) and is releasable to the National Technical Information Service (NTIS). At NTIS, it will be available to the general public, including foreign nations.

APPROVAL STATEMENT

This report has been reviewed and approved.

Elton R. Thompson

ELTON R. THOMPSON
Project Manager, Research Division
Directorate of Test Engineering

Approved for publication:

FOR THE COMMANDER

Robert W. Crossley

ROBERT W. CROSSLEY, Lt Colonel, USAF
Acting Director of Test Engineering
Deputy for Operations

REPORT DOCUMENTATION PAGE		READ INSTRUCTIONS BEFORE COMPLETING FORM
1. REPORT NUMBER AEDC-TR-79-49	2 GOVT ACCESSION NO	3 RECIPIENT'S CATALOG NUMBER
4. TITLE (and Subtitle) MEASUREMENTS IN THE TURBULENT BOUNDARY LAYER AT CONSTANT PRESSURE IN SUBSONIC AND SUPERSONIC FLOW, PART II. Laser-Doppler Velocity Measurements.		5 TYPE OF REPORT & PERIOD COVERED Final Report - May 1975 - February 1978 6. PERFORMING ORG. REPORT NUMBER JPL Publication 79-41
7. AUTHOR(s) Paul E. Dimotakis, Donald J. Collins, and Daniel B. Lang		8. CONTRACT OR GRANT NUMBER(s) F44620-75-C-0007 MIPR-EY 7483-76-0003 MIPR-EY 7483-76-0009
9 PERFORMING ORGANIZATION NAME AND ADDRESS Jet Propulsion Laboratory 4800 Oak Grove Drive Pasadena, California 91103		10. PROGRAM ELEMENT, PROJECT, TASK AREA & WORK UNIT NUMBERS Program Element 65807F
11 CONTROLLING OFFICE NAME AND ADDRESS Arnold Engineering Development Center/OIS Air Force Systems Command Arnold Air Force Station, Tennessee 37389		12. REPORT DATE July 1979 13 NUMBER OF PAGES 87
14 MONITORING AGENCY NAME & ADDRESS (if different from Controlling Office) Air Force Office of Scientific Research/NA Bolling AFB, DC 20332		15. SECURITY CLASS (of this report) UNCLASSIFIED 15a DECLASSIFICATION/DOWNGRADING SCHEDULE N/A

16 DISTRIBUTION STATEMENT (of this Report)

Approved for public release; distribution unlimited.

17 DISTRIBUTION STATEMENT (of the abstract entered in Block 20, if different from Report)

18 SUPPLEMENTARY NOTES

Available in DDC

19 KEY WORDS (Continue on reverse side if necessary and identify by block number)

turbulent boundary layer
Reynolds stresses
mean-flow scaling
laser-Doppler velocimeter

20 ABSTRACT (Continue on reverse side if necessary and identify by block number)

Experiments have been carried out using laser-Doppler velocimetry in conjunction with Pitot and surface-friction instrumentation for the measurement of the mean flow, the velocity fluctuations, and the Reynolds stresses in turbulent boundary layers at constant pressure in subsonic and supersonic flows. Two facilities were used for these studies. In one facility, data were obtained on a flat plate at $M_e = 0.1$, with $Re_\theta = 6600$. In the other, data were

DD FORM 1 JAN 73 1473 EDITION OF 1 NOV 65 IS OBSOLETE

20. ABSTRACT (Continued)

obtained on an adiabatic nozzle wall at M_e = 0.6, 0.8, 1.0, 1.3, 2.2 with Re_θ = 23,000 and 40,000. Part I of this work was a detailed analysis of the mean flow as observed using Pitot-tube, Preston-tube, and floating-element balance instrumentation. The present work (Part II) is a description of both the mean and the fluctuating components of the flow, and of the Reynolds stress as observed using a dual forward-scattering laser-Doppler velocimenter. A detailed description of the instrument, and of the data analysis techniques, have been included in order to fully document the data. A detailed comparison is made between the laser-Doppler results and those presented in Part I, and an assessment is made of the ability of the laser-Doppler velocimeter to measure the details of the flows involved.

Preface

This report represents the results of one phase of research carried out at the Jet Propulsion Laboratory of the California Institute of Technology, under Contract NAS 7-100. The work described in this report was supported by the United States Air Force, Office of Scientific Research, under Contracts F 44620-75-C-0007 and F 44620-76-C-0046; by the Arnold Engineering Development Center, under MIPR EY 7483-76-0003 and EY 7483-76-0009, Program Element No. 65807F; and by the California Institute of Technology, President's Fund, under Grant PF-075.

The authors are indebted to Professor Donald Coles for his continued assistance in this project and to Dr. Steven Barker, whose early participation contributed substantially to the final optics design. We would also like to acknowledge the assistance of Mr. George Tennant in assembling the optical system, and of Mr. Harold Holway and the crew of the J.P.L. 20-inch wind tunnel for their assistance in what may have been the final test to be conducted in that facility.

Contents

Part II. Laser-Doppler Velocity Measurements

Contents (Cont.)

I. Introduction

The turbulent boundary layer at constant pressure has been the subject of experimental and theoretical investigations for many years, and provides a well documented flow for the assessment of experimental techniques. These investigations have shown that for the incompressible turbulent boundary layer, the turbulent shearing stress can be measured directly or can be calculated from the distribution of mean velocity with the aid of well-established similarity laws. For compressible flows, however, measurements of the Reynolds stresses are rare, and interpretation of the results is difficult. Recent measurements by Johnson and Rose (1973), Yanta and Lee (1974), and by Abbiss (1976) have used laser-Doppler velocimetry techniques to make direct measurements of the Reynolds stress in turbulent boundary layers with free-stream Mach numbers in the range 1.5 to 3.0. However, a serious anomaly is exhibited by these measurements in that the maximum value of $-\rho\overline{u'v'}$ occurs much further from the wall than is reasonable for flow at constant pressure. This anomaly has been discussed by Sandborn (1974), who supports the conjecture by some of the authors cited that density fluctuations may contribute substantially to the turbulent stresses near the wall. This conjecture is in direct opposition to the conclusion by Morkovin (1961) that effects of density fluctuations should be small compared to effects of variations in mean density for Mach numbers up to 4 or 5.

The purpose of the present experiments is to obtain redundant data over a substantial range of Mach numbers (M_e = 0.1 to 2.2), in an effort to resolve the anomaly in turbulent shearing stress. The low-speed experiments were performed in the boundary layer on a flat plate model in the GALCIT* Merrill

*Graduate Aeronautical Laboratories of the California Institute of Technology.

wind tunnel at a free-stream Mach number $M_e \approx 0.1$. The high-speed experiments were performed in the ceiling boundary layer of the J.P.L.† 20-inch wind tunnel at Mach numbers $0.6 \leq M_e \leq 2.2$.

The flow was documented by conventional means using a Pitot tube, which was traversed through the boundary layer, to measure the mean flow. In addition, surface-friction measurements were made using both a floating-element balance and a Preston tube. The mean-flow scaling suggested by Van Driest (1955) was applied to the data, to test the adequacy of a single similarity formulation for both compressible and incompressible flow. The shearing stress was computed from the mean flow as part of the analysis. The details of these experiments have been discussed in Part I of this report by Collins, Coles and Hicks (1978).

In the present report, the instrumentation, data acquisition and analysis for laser-Doppler velocity measurements in the same flows are described. Measurements of $\bar{u}$, $\bar{v}$, $\overline{u'^2}$, $\overline{v'^2}$ and the Reynolds stress $-\rho\overline{u'v'}$ were made over the full Mach number range. These measurements are discussed and compared to the results for the mean flow presented in Part I of this work.

II. Measurement Considerations at High Speeds

The use of laser-Doppler velocimetry techniques in high-speed flows unavoidably results in very high frequency signals. Figure 1 is a plot of the Doppler frequency

$$\nu_D = \frac{2 \sin\theta/2}{\lambda} u_\perp \,, \tag{1}$$

†Jet Propulsion Laboratory

as a function of the flow velocity $u_\perp$ with the beam separation angle θ as a parameter. For these computations, the wavelength has been assumed to be $\lambda = 0.5145$ μm, corresponding to an argon-ion laser.

A reduction in the beam separation angle θ, in order to achieve a reduction in the signal frequency, results in a reduction in the number of fringes within the measurement ellipsoid, and a consequent reduction in the measurement accuracy. The interesting beam pair produces a set of virtual fringes whose spacing is given by

$$s = \frac{\lambda}{2 \sin\theta/2} \quad . \tag{2}$$

Because the (TEM_{oo}) Gaussian beam radius at the focus is given by

$$w_o = \frac{\lambda R}{\pi w} \quad , \tag{3}$$

where R is the beam wavefront radius of curvature after the focusing lens ($R \sim f$ = lens focal length), and w is the $1/e^2$ intensity envelope radius at the focusing lens, the resulting number of fringes is then given by (e.g., Dimotakis (1976))

$$N_f = 4 \frac{w_o}{\lambda} \tan\theta/2 \quad . \tag{4}$$

The number of fringes, N_f, is plotted in Figure 2 as a function of the focal volume diameter $2 w_o$ with the angle θ as a parameter for a wavelength $\lambda = 0.5145$ μm. As can be seen from Figure 2, spatial resolution considerations place a lower bound on the angle θ, presenting a criterion which

conflicts with the requirement to keep the resulting Doppler frequencies small.

Other difficulties arise if the Doppler frequencies are permitted to be large. In addition to the problems of handling high frequencies per se, the relative accuracy $\delta u/u$ with which the velocity of a single particle can be measured is never less than the ratio of the processor clock period, τ_c, to the total flight time Δt that is used for the measurement, i.e.,

$$\frac{\delta u}{u} > \frac{\tau_c}{\Delta t} \tag{5}$$

By way of example, a processor with a clock frequency of 100 MHz ($\tau_c = 10^{-8}$ sec) can measure the velocity of a Mach $\sim$ 2 particle in air ($u_\perp \sim 530$ m/sec) in a 800 μm diameter focal volume to about $\sim$ 0.7%.

In addition to these considerations, which would limit the accuracy even if the measurement environment was noise free, other factors become important at high velocities by decreasing the signal-to-noise ratio of a single reading. As the flow velocities become higher, smaller particles are required to minimize problems of particle lag. This results in rapidly decreasing scattering cross-sections (Born and Wolf (1975)) and consequent signal intensities. In addition, as the velocity increases, the scattering particle spends less time in the focal volume. As a result, even though the number of scattered photons per second remains constant, proportional to the scattering cross-section, fewer total photons are collected by the detecting optics. An equivalent way of analyzing this problem is to consider the noise bandwidth that must be utilized as the velocities, and resulting

Doppler frequencies, increase. For a shot-noise limited detection process, the noise power increases proportionally to the bandwidth that is accepted by the processing electronics. Consequently, using the same particles, the signal-to-noise ratio will decrease as the velocity increases.

III. Scattering Particles

A. Particle Lag

The extent to which the measurement of particle velocity represents the fluid velocity is, of course, a separate issue. If the Lagrangian fluctuation frequencies in the fluid are small compared to the reciprocal of a characteristic particle response time, τ_p, the particles are expected to follow those fluctuations.

For small solid particles in gas flows, the equation of motion in a Lagrangian frame can be approximated by

$$\frac{d}{dt} u_p + \frac{1}{\tau_p} u_p = \frac{1}{\tau_p} u_f \quad . \tag{6}$$

If the particle Reynolds number

$$Re_p \equiv \frac{|u_p - u_f|}{\nu} d_p \quad , \tag{7}$$

is small, and the flow can be described by the continuum equations, we have the classical Stokes flow for a spherical particle for which the drag coefficient is $C_D = 24/Re_p$. The particle response time is then given by

$$\tau_p = \frac{d_p^2}{18} \left(\frac{\rho_p}{\mu}\right) = \frac{d_p^2}{18\nu} \left(\frac{\rho_p}{\rho_f}\right) \tag{8}$$

which is independent of the fluid density. A plot of the particle response time as a function of the particle diameter is given in Figure 3 for dibutyl phthalate aerosol particles in air.

In order to estimate the fluctuation frequencies to which a particle will be subjected, it is useful to examine the Eulerian fluid motions in the turbulent boundary layer. From the measurements of Klebanoff (1954) in a boundary layer at constant pressure, and from the measurements of Perry and Abell (1975; 1977) in pipes, the behavior of the Eulerian velocity fluctuation spectrum can be inferred. These results give spectra which can be described by

$$\frac{S_{uu}(\omega,y)}{\overline{u'^2}(y)} \simeq \frac{\pi\delta}{u(y)} f_o\left[\frac{\omega\delta}{u(y)}\right] \tag{9}$$

for the wake region, and

$$\frac{S_{uu}(\omega,y)}{\overline{u'^2}(y)} = \frac{\pi y}{u(y)} f_1\left[\frac{\omega y}{u(y)}\right] \tag{10}$$

in the inner portion of the boundary layer, but outside the sublayer. These spectra then result in expected frequencies given by

$$\langle\omega\rangle_\delta = \text{const.} \frac{u(y)}{\delta} \quad , \tag{11}$$

in the wake region, and

$$\langle\omega\rangle_y = \text{const.} \frac{u(y)}{y} \quad , \tag{12}$$

in the boundary layer interior. Consequently, particles above the sublayer should track the flow well, provided that

$$\frac{\tau_p u(y)}{y} \lesssim 1 \quad , \tag{13}$$

$$\frac{\tau_p a_e}{\delta} \lesssim \frac{1}{M_e} \left[\frac{y/\delta}{u(y)/u_e}\right] . \tag{14}$$

Substituting Equation (8) for τ_p, we obtain an upper bound on the particle diameter for the particles to track the flow,

$$d_p < d_{p_{max}} \approx \frac{4.83}{M_e^{\frac{1}{2}}} \mu m \quad , \tag{15}$$

for di-butyl phthalate aerosol in air at 25°C.

A prediction of Equation (12) is that the turbulent wavenumbers $k \sim \omega/u$ increase as the wall is approached,

$$k \sim \frac{const.}{y} . \tag{16}$$

This result is confirmed qualitatively by the photograph in Figure 4 in which the turbulent boundary layer on the surface of a water channel has been made visible using a thick suspension of aluminum flakes which preferentially align with the local strain field. The photograph was taken in the GALCIT low-speed water channel by Brian Cantwell and is reproduced here with his permission. The Reynolds number for this photograph, based on x,

was 10^6. The monotonic decrease in scale size as the wall is approached is quite evident. These observations, and the results of Equation (12) are consistent with the usual mixing-length hypotheses made for the outer layer by Prandtl (1942), and are consistent with the hypothesis for the region closer to the wall, but outside the viscous layer by von Kármán (1930).

In the interior of the boundary layer, the quantity in the brackets in Equation (14) is bounded by the relation

$$\frac{y/\delta}{u(y)/u_e} > \frac{u_e/u_\tau}{\delta u_\tau/\nu_w} \equiv \frac{u_e^+}{\delta^+} , \tag{17}$$

where u_τ is the friction velocity defined as

$$u_\tau \equiv (\tau_w/\rho_w)^{\frac{1}{2}} \tag{18}$$

The ratio u_e^+/δ^+ has been shown by Coles (1968) to be a function of Re_θ for incompressible flows with zero pressure gradient. The square root of this quantity is plotted in Figure 5, for the range of Re_θ covered by the present measurements ($8 \times 10^3 < Re_\theta < 4 \times 10^4$). The data for this figure are taken from Table 4 of Collins, Coles and Hicks (1978). These data are compared in Figure 5 to a straight line fit given by the emperical relation

$$\sqrt{u_e^+/\delta^+} \simeq f(Re_\theta) = 5.01\ Re_\theta^{-0.435} . \tag{19}$$

In writing the lower bound in Equation (17), effects of compressibility have been ignored. Using the numerical result of Equations (15) and (19), we then have

$$d_p < d_{p_{max}} \simeq \begin{cases} \dfrac{4.83}{M_e^{\frac{1}{2}}} \left(\dfrac{y}{\delta}\right)^{\frac{1}{2}} \ (\mu m) & ; \quad \text{far from the sublayer} \\ \dfrac{24.2}{M_e^{\frac{1}{2}} Re_\theta^{0.435}} & ; \quad \text{near but outside the sublayer .} \end{cases} \tag{20}$$

By way of example, a flow of $M_e \sim 1$ requires particles less than 1.5 μm in diameter to track the fluctuations at $y/\delta \sim 0.1$.

B. Techniques for Seeding the Flow

The particle generator for the present experiments used a Laskin nozzle type construction to generate a poly-dispersed aerosol of di-butyl phthalate. Particles greater than 1 μm in diameter were effectively removed by an impact plate incorporated in the design. The resulting particle size distribution, measured using both a cascade impactor and a multi-channel particle analyzer, is shown in Figure 6. These results indicate little contribution to the number density for sizes greater than 1 μm. While little is known about the distribution below 0.4 μm, it was possible to ascertain that no particles with a diameter less than 0.1 μm were present.

Two different methods were used to introduce particles into the flow depending on the flow facility that was used. For the high-speed measurements ($0.6 \lesssim M_e \lesssim 2.2$), which were conducted in the JPL 20-inch wind tunnel, it was necessary to seed the flow by introducing the particles into the settling chamber between the last turbulence screen and the contraction section. The particles were introduced through a tube which protruded 5 cm vertically into the settling chamber from above. Holes were drilled into the tube along

the stagnation line as well as the rear side at ± 30° with respect to the flow vector. Using this technique, data rates in excess of 50,000 samples per second were achieved. Preston-tube measurements obtained with and without particles indicate no detectable influence of the introduction of particles on the surface friction and therefore, probably, on the mean flow.

For the low-speed measurements in the Merrill wind tunnel ($M_e \simeq 0.1$), although some naturally occurring particles were present, the flow was seeded using the same aerosol generator in order to increase the data rate and to control the scattering particle size distribution. For these measurements the particles were injected through a tube spanning the test section located downstream of the boundary-layer plate, providing a uniform distribution of particles throughout the test section. In practice, the adjustment of the rate at which particles were introduced proved difficult because the characteristic time was of the order of several minutes for equilibrium with particle losses. As a consequence, the particle number density changed during the time required for a traverse through the boundary layer. Using this seeding technique, data rates in excess of 2,000 samples/sec were achieved at low speeds.

C. The Distribution of Particles

The particle number density was measured by counting the average frequency of occurrence of valid data from the processing electronics. These data are a measure of the mean particle flux $\langle nu \rangle$. Assuming that correlations between the scattering particle number density and the streamwise velocity are small, then

$$\langle n \rangle = \frac{\langle nu \rangle}{\langle u \rangle} \tag{21}$$

gives the mean value of the particle number density.

It is an unfortunate consequence of this measurement technique that the measured value of the particle flux $\langle nu \rangle$ decreases with the signal-to-noise ratio of the experiment. The most common cause of a decrease in the signal-to-noise ratio in the high-speed flow experiments has been attributed to the random occurrence of oil filaments on the windows through which the observations were made. Imperfections in the lucite windows in the Merrill wind tunnel had a similar effect on the measured particle flux. In addition, a more serious problem arose in the low-speed measurements, where the particle flux was a slowly-varying function of time.

The resulting distribution of particle number density through the boundary layer is shown in Figures 7, 8 and 9, in which the particle number density has been normalized by the local fluid density in order to account for the effects of compressibility. These data are further normalized by their maximum value in the boundary layer to eliminate the effects of differing injection rates.

The loss mechanisms of the scattering particles from the boundary layer are important in understanding the resulting laser-Doppler observations. For the high-speed experiments, the particle distribution was initially both spatially and temporally approximately uniform over a restricted volume of fluid in the settling chamber. The particle distribution in the outer portion of the boundary layer is then determined by the diffusion of the passive scalar into the outer flow. In addition to diffusion, the entrainment of fluid into the boundary layer from the free stream by the mechanism of large-scale eddy engulfment contributes substantially to the structure of the particle number density profiles. Because the entrained fluid contains no particles,

the measured distributions shown in Figures 7 and 8 exhibit a rapid decay away from the wall, with the particle number density falling to zero in the outer portion of the boundary layer. This entrained fluid is underrepresented in the Doppler measurements because of the loss of statistical weight.

As the wall is approached, the particle number density, normalized by the local fluid density, decays more rapidly than the velocity as a result of the loss of particles to the wall. This loss to the wall is evident from the observation of an oil film on the test surface.

IV. Optics and Measurement Geometry

A. Position Measurement

The present experiments utilized the laser-Doppler velocimeter in the single particle, dual forward-scatter mode. The instrument was mounted on a vibration isolated, two-axis traverse which permitted surveys up to 75 cm in the streamwise direction, and 20 cm in the direction normal to the test plate. For measurements in the JPL 20-inch wind tunnel, the instrument was mounted on top of the wind tunnel test section, as depicted in Figure 10. For measurements in the GALCIT Merrill wind tunnel, the traverse was suspended from the ceiling of the laboratory, and was not fixed relative to the test plate.

The vertical position was sensed by means of a helipot mounted on the vertical traverse and was repeatable to better than 0.005 cm. The origin for the vertical position measurements was estimated by placing a razor blade of known width normal to the test surface at the location of the focal volume. The origin was then measured by determining the half intensity of transmission as a function of position of one of the beams.

In practice, establishing the origin, to within the accuracy warranted by the data, by direct measurement proved difficult for a variety of reasons. These inherent difficulties in measuring the position of the wall, relative to the LDV traversing mechanism necessitated establishing the origin in y using the data for the mean-velocity profile. This was accomplished by a least-squares fit of the mean-velocity data to the law of the wall and the law of the wake in the form

$$u^+ = \frac{1}{\kappa} \ln y^+ + c + \frac{2\Pi}{\kappa} \sin^2 Y \quad , \tag{22}$$

where

$$u^+ = u/u_\tau \quad , \tag{23}$$

$$y^+ = (y - y_o) \frac{u_\tau}{\nu} \quad , \tag{24}$$

$$Y = (y - y_o) \frac{\pi}{2\delta} \quad , \tag{25}$$

and where y_o is the small offset of the position of the wall required to establish the proper origin.

For this purpose, a least-squares analysis was performed to determine the parameters u_τ, Π and y_o with $\kappa = 0.41$ and $c = 5.0$ given, and δ was computed as a constraint imposed by the local friction law,

$$u_e^+ = \frac{1}{\kappa} \ln \delta^+ + c + \frac{2\Pi}{\kappa} \tag{26}$$

The technique for this analysis is outlined in Part I of this work by Collins, Coles and Hicks (1978) in conjunction with the mean-flow data

presented there. The results of this procedure lead to corrections y_o of the order of the focal volume diameter. In particular, the maximum correction was 0.18 cm for one case of the high-speed data and 0.075 cm for the low-speed flow measurements.

B. Transmitting Optics

The light source for this instrument was a Coherent Radiation Model 52B, 4-watt argon-ion laser. The laser was operated single line at 0.5145 μm and used an oven stabilized etalon to provide a single-mode beam. It was mounted on the tubular support structure for the optics as shown in Figure 10. This configuration ensures that the focal volume remains unchanged as the assembly is traversed and also that the relative alignment between the transmitting and receiving optics is preserved to within a few percent of the focal-volume diameter.

The laser output beam was directed into the vertical support tube for the transmitting optics by means of two separate mirrors in order to preserve the proper polarization of the beam. The transmitting optics cell contains a fixed mirror to direct the beam into the horizontal plane maintaining a vertical polarization vector. The beam is then split into two beams of unequal intensity by reflection from the front and rear surfaces of the first of two multiply-coated beam splitters. The resulting beam pair is then transmitted through a second multiply-coated beam splitter which divides the stronger beam into two beams of equal intensity. This arrangement results in three parallel beams of approximately equal intensity which form a right isosceles triangle whose base is nominally parallel to the test surface. The three output beams are then focused in the center of the tunnel by a 1.0 meter focal length, antireflection coated lens, to a common focal volume $\sim$ 0.8 mm in

diameter. The optical axis intercepts the test plate from below at an angle of ~ 1:100 in order to permit measurement of the boundary layer close to the surface of the polished test plate.

The resulting focal volume contains three independent sets of virtual fringe planes correspondingly perpendicular to the $\underline{u}$, $(\underline{u} + \underline{v})/\sqrt{2}$ and $(\underline{u} - \underline{v})/\sqrt{2}$ velocity vectors. The geometry of the three beam pairs, and actual photographs of the fringes formed by each beam pair, are shown in Figure 11. By selectively blocking one of the three beams, any one of the three velocity components can be examined without a change in the focal-volume geometry. This method we consider superior to the more common one of rotating a single beam pair in the desired orientation which, in our experience, cannot easily be done with sufficient reproducibility and without slight displacements of the focal volume.

C. Geometry of the Intersection Volume

The three intersecting beams, taken in pairs, define three planes, along which the measurements were taken. Even though considerable care was taken to orient these planes at 0° and $\pm 45^\circ$ with respect to the wall, the small deviations that were measured were taken into account in the data analysis.

The subtended angles between the beam pairs were measured by two different methods on two different occasions and found to be within ~ 0.3% of the values:

$$\begin{aligned} \theta_1 \left\{ \underline{u} \text{ measurement} \right\} &= 0.02112 \text{ rad} \\ \theta_2 \left\{ \frac{1}{\sqrt{2}} (\underline{u} + \underline{v}) \text{ measurement} \right\} &= 0.01490 \text{ rad} \\ \theta_3 \left\{ \frac{1}{\sqrt{2}} (\underline{u} - \underline{v}) \text{ measurement} \right\} &= 0.01424 \text{ rad}. \end{aligned} \tag{27}$$

Thus, $\theta_2 \simeq \theta_3 \simeq \theta_1/\sqrt{2}$ define a nearly isosceles triangle as illustrated in Figure 11.

As a consequence of the requirement to isolate the traversing mechanism from vibrations, the relative orientation between the hypotenuse of the triangle and the wall (angle ϕ, Figure 12) had to be determined by a separate measurement for each profile. This was accomplished by permanently mounting a second razor blade to one side of the test plate with its edge aligned with the surface of the plate. The relative orientation for the optics could then be determined by measuring the offset between the two beams forming the triangle hypotenuse. This angle ϕ is small in every case but must be accurately known to estimate any quantities that involve v, the velocity component normal to the wall.

Using the geometry as defined in Figure 12, we have from the law of cosines,

$$\left.\begin{aligned} \cos\alpha &= \frac{\theta_2^2 + \theta_3^2 - \theta_1^2}{2\,\theta_2\theta_3}\,, \\ \cos\beta &= \frac{\theta_3^2 + \theta_1^2 - \theta_2^2}{2\,\theta_3\theta_1}\,, \\ \text{and}\quad \cos\gamma &= \frac{\theta_1^2 + \theta_2^2 - \theta_3^2}{2\,\theta_1\theta_2}\,. \end{aligned}\right\} \tag{28}$$

Assuming now that the velocity vector in two dimensions can be defined by its components in the three directions defined in Figure 12, we have that the three measured components are given by

$$\left.\begin{aligned} u_1 &= b_{11}u + b_{12}v \\ u_2 &= b_{21}u + b_{22}v \\ u_3 &= b_{31}u + b_{32}v \end{aligned}\right\} \tag{29}$$

where

$$\left.\begin{aligned} b_{11} &= \cos\phi & b_{12} &= \sin\phi \\ b_{21} &= \cos(\gamma + \phi) & b_{22} &= \sin(\gamma + \phi) \\ b_{31} &= \cos(\beta - \phi) & b_{32} &= -\sin(\beta - \phi) \end{aligned}\right\} . \tag{30}$$

Equations (29) form a redundant set, and can be used to check the validity of the data. In particular, since $\sin(\beta + \gamma) = \sin\alpha$, we must have

$$\langle u_1 \rangle \sin\alpha = \langle u_2 \rangle \sin\beta + \langle u_3 \rangle \sin\gamma . \tag{31}$$

Recall from Equation (1) that

$$\nu_{D_i} = \frac{2 \sin\theta_i/2}{\lambda} u_i \simeq \frac{\theta_i}{\lambda} u_i , \tag{32}$$

so that the consistency Equation (31) becomes

$$\langle \nu_{D_1} \rangle = \langle \nu_{D_2} \rangle + \langle \nu_{D_3} \rangle . \tag{33}$$

Alternatively, Equations (29) can be solved in pairs to obtain two independent estimates of $\langle u \rangle$ and $\langle v \rangle$ at each location,

$$\begin{pmatrix} b_{11} & b_{12} \\ b_{21} & b_{21} \end{pmatrix} \times \begin{pmatrix} \langle u_I \rangle \\ \langle v_I \rangle \end{pmatrix} = \begin{pmatrix} \langle u_1 \rangle \\ \langle u_2 \rangle \end{pmatrix} , \tag{34}$$

and

$$\begin{pmatrix} b_{11} & b_{12} \\ b_{31} & b_{32} \end{pmatrix} \times \begin{pmatrix} \langle u_{II} \rangle \\ \langle v_{II} \rangle \end{pmatrix} = \begin{pmatrix} \langle u_1 \rangle \\ \langle u_3 \rangle \end{pmatrix} \tag{35}$$

Inverting Equations (34) and (35), we then have

$$\left.\begin{aligned} \langle u_I \rangle &= \frac{\langle u_1 \rangle \sin(\gamma + \phi) - \langle u_2 \rangle \sin\phi}{\sin\gamma} \\ \langle v_I \rangle &= \frac{\langle u_2 \rangle \cos(\phi) - \langle u_1 \rangle \cos(\gamma + \phi)}{\sin\gamma} \end{aligned}\right\} \tag{36}$$

and

$$\left.\begin{aligned} \langle u_{II} \rangle &= \frac{\langle u_1 \rangle \sin(\beta - \phi) + \langle u_3 \rangle \sin\phi}{\sin\beta} \\ \langle v_{II} \rangle &= \frac{\langle u_1 \rangle \cos(\beta - \phi) - \langle u_3 \rangle \cos\phi}{\sin\beta} \end{aligned}\right\} \tag{37}$$

The final values for $\langle u \rangle$ and $\langle v \rangle$ were then estimated by averaging the two independent estimates,

$$\left.\begin{aligned} \langle u \rangle &= \frac{1}{2}\left(\langle u_I \rangle + \langle u_{II} \rangle\right) \\ \langle v \rangle &= \frac{1}{2}\left(\langle v_I \rangle + \langle v_{II} \rangle\right) \end{aligned}\right\} . \tag{38}$$

Using Equations (29), we can also relate the mean-square fluctuations of the measured velocity components, to $\langle u'^2 \rangle$, $\langle v'^2 \rangle$ and $\langle u'v' \rangle$. In

particular, we have

$$\left.\begin{aligned}
\langle u'^2_1 \rangle &= b_{11}^2 \langle u'^2 \rangle + b_{12}^2 \langle v'^2 \rangle + 2\, b_{11} b_{12} \langle u'v' \rangle \\
\langle u'^2_2 \rangle &= b_{21}^2 \langle u'^2 \rangle + b_{22}^2 \langle v'^2 \rangle + 2\, b_{21} b_{22} \langle u'v' \rangle \\
\langle u'^2_3 \rangle &= b_{31}^2 \langle u'^2 \rangle + b_{32}^2 \langle v'^2 \rangle + 2\, b_{31} b_{32} \langle u'v' \rangle
\end{aligned}\right\} \tag{39}$$

Note that while Equations (29) are redundant, Equations (39) are not, except for special choices of β, γ and ϕ. Inverting Equations (39), we then have

$$\left.\begin{aligned}
\langle u'^2 \rangle &= C_{11} \langle u'^2_1 \rangle + C_{12} \langle u'^2_2 \rangle + C_{13} \langle u'^2_3 \rangle \\
\langle v'^2 \rangle &= C_{21} \langle u'^2_1 \rangle + C_{22} \langle u'^2_2 \rangle + C_{23} \langle u'^2_3 \rangle \\
\langle u'v' \rangle &= C_{31} \langle u'^2_1 \rangle + C_{32} \langle u'^2_2 \rangle + C_{33} \langle u'^2_3 \rangle
\end{aligned}\right\} , \tag{40}$$

where the C_{ij} matrix is given by,

$$\left.\begin{aligned}
C_{11} &= \sin(\beta + \gamma) \sin(\beta - \phi) \sin(\gamma + \phi)/\Delta \\
C_{12} &= -\sin\beta \sin(\beta - \phi) \sin\phi/\Delta \\
C_{13} &= \sin\gamma \sin(\gamma + \phi) \sin\phi/\Delta
\end{aligned}\right\}$$

$$\left.\begin{aligned}
C_{21} &= -\sin(\beta + \gamma) \cos(\beta - \phi) \cos(\gamma + \phi)/\Delta \\
C_{22} &= \sin\beta \cos(\beta - \phi) \cos\phi/\Delta \\
C_{23} &= \sin\gamma \cos(\gamma + \phi) \cos\phi/\Delta
\end{aligned}\right\} \tag{41}$$

$$\left.\begin{aligned} C_{31} &= -\frac{1}{2}\sin(\beta+\gamma)\sin(\beta-\gamma-2\phi)/\Delta \\ C_{32} &= \frac{1}{2}\sin\beta\sin(\beta-2\phi)/\Delta \\ C_{33} &= -\frac{1}{2}\sin\gamma\sin(\gamma+2\phi)/\Delta \end{aligned}\right\}\Bigg\}\,,$$

and where

$$\Delta = \sin\beta \cdot \sin\gamma \cdot \sin(\beta+\gamma)\ . \tag{42}$$

D. Receiving Optics

The optical axis for the receiving optics is aligned at an angle of $\sim 7.5^{\circ}$ with respect to the test-plate surface, thus permitting a full view of the focal volume throughout the boundary layer. This inclination of both the transmitting and the receiving optics with respect to the test surface results in a reduction of the spanwise extent of the focal volume. The collecting lenses consist of a pair of 15.24 cm diameter, f/5 achromats which have been anti-reflection coated and are mounted back-to-back in a common cell. This configuration provides a 1:1 imaging system that was measured to be approximately twice diffraction limited. The collected light cone is directed by a 10 cm diameter multi-layer dielectric coated mirror into a 0.05 cm diameter pinhole which spatially filters the collected light that is accepted by the photomultiplier assembly. The photomultiplier assembly consists of a focusing mount with a 20 mm focal length, f/5 coated lens, a 30Å wide 0.5145 μm filter and magnetic lensing to restrict the photocathode of an EMI 9813B photomultiplier tube. The photomultiplier tube output is coupled directly to a low-noise fast rise-time preamplifier, constructed inside the tube housing at the base of the photomultiplier tube. The photodetection system was designed with a frequency response in excess of 50 MHz.

The effective focal-volume diameter is defined by the pinhole in the receiving optics and is therefore equal to ~ 0.05 cm.

Oscilloscope traces of raw signals from the output of the preamplifier at the base of the photomultiplier are included in Figure 13. These photographs are multiple exposures taken of particle bursts at the highest recorded velocities of $M_e \sim 2.2$ ($Re_\theta \sim 4 \times 10^4$) at the edge of the boundary layer. The frequency of the u-component signal is about 26 MHz. The frequency of the (u + v)-component signal is almost exactly one-half the u-component frequency. This feature, which will be discussed later, is exploited by the processing scheme. Typical signal-to-noise ratios of 15-20 db were measured at these velocities.

V. Signal Processing and Data Acquisition

The output of the photomultiplier, coupled through the integral preamplifier, was monitored on a HP 8553B/8552B wave analyzer which was also used to align the optics and tune the entire system by maximizing the signal-to-noise ratio of the Doppler signal. This signal was filtered by a two-pole low-pass filter in order to eliminate the substantial shot noise above the Doppler frequencies. The pedestal, resulting from the dual-scatter optics, is not removed by this processing scheme.

A. The LDV Processor

The filtered output signal is fed into the LDV processor (Dimotakis and Lang (1977)) depicted in block diagram in Figure 14. The various components of this processor are described in the following paragraphs.

1. The Analog Input Processor

The Analog Input Processor defines a reference level V_0 and two symmetric levels $V_0 - V_L$, $V_0 + V_L$ about V_0 as shown in Figure 15a. In addition, a fourth

level V_M can also be defined which must be higher than $V_0 + V_L$. The amplitudes V_0, V_L and V_M, as well as the polarity, are independently selectable. The filtered Analog INput (AIN) must cross $V_0 - V_L$ from below and then $V_0 + V_L$ from below, in that order, before the Digital INput (DIN) is raised. A subsequent crossing of V_0 from above will cause DIN to go low. This test sequence must be passed by the analog input AIN on every cycle, otherwise the burst is rejected, the logic is reset, and the processor waits for the next burst. If the analog input AIN exceeds V_M at any time during the burst, the burst is rejected, the logic is reset, and the processor waits for the next burst (cf. Figure 15a). Thus the amplitudes V_0, V_L and V_M specify the range of particle sizes accepted by the processor for the measurement. The frequency of the signal DIN can be prescaled (cf. Figure 15b) to produce the signal DIN′ which has one negative slope for every m negative slope of DIN. The constant m is front panel selectable and can be set to 1, 2, 4 or 8. The Analog Input Processor is designed with high-speed ECL circuitry and stripline technology with a maximum Doppler frequency of 170 MHz.

2. The Digital Input Processor

The prescaled digital input DIN′ is subsequently processed by the Digital Input Processor. The negative slope of DIN′ fires a resettable one-shot T1 of duration τ_1, as illustrated in Figure 16. The negative slope of T1 fires a resettable one-shot of duration τ_2. The first negative slope of DIN′ also raises a signal G, which gates a 100 MHz crystal clock into the Flight Time (FT) counter, as illustrated in Figure 17. The next negative slope of DIN′, refires the one-shot T1, resets the T2 one-shot and generates a short TRansfer Pulse (TRP) which stores the FT buffer and increments the cycle counter (cf. Figures 16 and 17). If the T2 one-shot times out before it is reset, an error

flag is raised, the logic is reset and the processor waits for the next burst. As a consequence, the logic checks that every period of the prescaled digital input falls within predetermined limits. If τ is the period of the Doppler signal, we must have, as a consequence,

$$\tau_1 < m\tau < \tau_1 + \tau_2 \quad , \tag{43}$$

where m = 1, 2, 4, 8. The time intervals τ_1 and τ_2 are front panel selectable and cover the range 60 nsec $< \tau_1, \tau_2 <$ 3 msec. The maximum Doppler frequency that can be handled by the Analog and Digital Processors working in tandem is given by,

$$(\nu_D)_{max} = \frac{max(m)}{min(\tau_1)} = \frac{8}{60 \times 10^{-9}} = 130 \text{ MHz} \quad . \tag{44}$$

3. The Timer

The 100 MHz crystal clock is divided by 10 to form a 10 MHz time standard which is used as the clock for the timer, as illustrated in Figure 17. The timer, in turn, has a $\div 10^N$ prescaler which sets the time base. This increments a free running 32-bit counter which can be reset if required but is normally allowed to overflow. The gate signal G is inverted to form $\overline{G}$ and is used to latch the contents of the timer counter into the timer buffer, as illustrated in Figure 18. The purpose of this information is to record the real time of each scattering event, to permit the reconstruction of the velocity fluctuations in time (cf. Dimotakis and Brown (1975)). While the present data rate was often high enough ($\sim$ 50 kHz) to warrant an examination of the velocity fluctuations in time, it was decided not to include such data in the present report.

4. Performance and Operating Modes

The LDV processor operates at the theoretical performance of ± 1/2 clock count (10 nsec) in determining the flight time Δt_i of the i^{th} scattering particle. The overall measurement accuracy is of course limited by a variety of other factors such as optical precision, signal-to-noise of the signal at the processor input, etc. In all the high-speed cases ($M_e \gtrsim 0.8$), the finite frequency of the processor clock was the limiting factor in the velocity measurement accuracy of a single particle. The highest frequency that occurred was 27 MHz in the $M_e \simeq 2.2$ flow. This frequency was measured with an overall accuracy for a single particle of ~ 2%. A histogram from a 1,024 particle record taken in the free stream ($M_e \simeq 2.2$) of the flight time for 8 Doppler cycles, is depicted in Figure 19. It can be seen that ~ 2/3 of all the counts fall in one 10 nsec bin. At the lower velocities the limitations arose as a result of the combined effect of all the other sources of error. For the $M_e \sim 0.1$ measurements an accuracy of 0.5% for a single particle was achieved. It should be emphasized that while the accuracy for a single particle velocity measurement does not limit the accuracy with which mean velocities can be determined, it contaminates the measurement of the rms fluctuation levels.

The processor is capable of operating in a variety of modes. Two of the modes that were used in this work will be discussed.

In the first mode, a fixed number of cycles is stored in the Mode Logic circuitry and compared with the contents of the Cycle Counter after each TRP pulse (cf. Figures 16 and 17). When the two numbers match, the Count End (CEND) flag is raised which in turn lowers the GO disabling the system (cf. Figures 17 and 15a). The output is then read and the processor is

reset and waits for the next burst (dead time ~ 60 nsec). All the data for $M_e > 0.6$ (JPL 20-inch Wind Tunnel) were recorded in this mode. Eight cycles were counted for the beam pair at 0° (u_1 data) with the prescaler m set to 2. Four cycles were counted for the $\pm 45^\circ$ (u_2, u_3 data) beam pairs with the prescaler set to unity. The advantage of this scheme was that the digital processor saw the same frequencies and numbers of cycles for all configurations. This occurs for the present measurements because the projection of the velocity vector along the $\pm 45^\circ$ directions is approximately given by

$$u_2 \simeq u_3 \simeq \frac{u_1}{2^{\frac{1}{2}}} \quad , \tag{45}$$

and hence the resulting Doppler frequencies are given by

$$\nu_{D_2} \simeq \nu_{D_3} \simeq \frac{1}{2} \nu_{D_1} \quad . \tag{46}$$

This uniformity in the processing, allows all the signals to be processed with identical settings except for a change in the prescaler from 1 to 2. The particle velocity is then determined by reading the output of the FT counter which corresponds to the flight time of the particle for the fixed number of fringes specified.

In the second mode, the processor requires that a fixed number of cycles be reached or exceeded by the burst and records the flight time and number of cycles of the entire burst. The sequence depicted in Figure 15a represents such a mode where, assuming that each period of DIN passed the τ_1, τ_2 test, the end of the burst was determined by the Analog Input Processor. The flight time Δt that would have resulted from

such a burst is indicated on the figure while the output of the cycle counter would have been n = 3 (number of TRP pulses and also number of fringe plane intervals). Both n and Δt would be recorded in this mode and the velocity would be

$$u_{\perp} = \frac{ns}{\Delta t} \tag{47}$$

The data recorded at $M_e \sim 0.1$ (GALCIT Merrill Wind Tunnel) were acquired in this mode requiring at least four fringes for the $\pm 45^{\circ}$ data (u_2, u_3) and at least eight for the 0° data (u_1). Thus, in both modes, the same minimum number of fringes had to be crossed.

There are several important differences between the two modes. First, using the facility of the processor to recognize the end of the burst while retaining the previous valid measurement allows the total flight time to be used, instead of an arbitrary fraction, in determining the velocity component of interest. This improves the measurement accuracy in an obvious way. Second, the phase errors that are made in assigning equal phase to the crossings of the reference level V_0 by the signal are cancelled when the entire burst is used. Third, the sampling statistics are different between the two modes. In the first mode (fixed number of fringes), all we know is that the particle crossed at least that many. In the second mode (number of fringes unrestricted provided it exceeds a certain minimum) we know that the particle crossed exactly that many. The sampling bias is different for these two cases, as will be discussed in Section VI-B.

B. Output Formatting

The (i) flight time, (ii) total number of validated cycles and (iii) the real time are encoded by the processor into three 32-bit words as binary

coded decimals (BDC). These data serve as input to the subsequent formatting electronics which selected the four least significant decades of the flight time to form a sixteen-bit word and, depending on the fringe mode, either the sixteen bits of the real time for the fixed-fringe mode, or the number of fringe crossings, in the free-fringe mode. These data were then combined to form a single 32-bit word.

The asynchronous data from the processor were recorded in dual 1024 X 32-bit buffers. One buffer was filled asynchronously with the processor output while the second was clocked synchronously, as a sequence of 4 bits/word on a Kennedy Model 9100 digital tape deck. Each 1024 X 32-bit buffer constituted a 4K-bit record on tape. Several records were recorded at each station depending on the turbulence level and average data rate.

VI. Data Processing

In computing the Reynolds stress $-\rho\overline{u'v'}$ from the measured velocity data, it is necessary to estimate both the first and second moments of the data, and to extract relatively small differences between two large numbers. This necessitates a careful accounting of all random and systematic errors that result from spurious measurements. In the present experiments, such errors are caused by a finite signal-to-noise ratio, and appear as isolated counts when the measurements are treated in histogram form. Errors are also caused by LDV sampling bias and by both the finite clock period and by noise in the processing electronics and in the optics. Errors which arise as a result of the finite measurement volume have been found to only be important in the immediate vicinity of the wall, and have not been corrected in the present analysis. The correction of such errors would result in a correction of at most the first two data points adjacent to the wall, for which we have the least confidence, and would not affect the conclusions presented.

A. Histogram Pruning

The data from the present experiments were recorded as multiple records of 1024 individual realizations of the three instantaneous velocity components $\underline{u}$, $\underline{u} + \underline{v}$, $\underline{u} - \underline{v}$. These data were processed by forming a separate histogram for each record, and subsequently performing the statistical computations using the resulting histograms. For the high-speed flow experiments, the data were recorded in the fixed-fringe mode and the histograms were formed as a function of the integer flight time Δt_i. The low-speed measurements were recorded in the free-fringe mode for which the flight time was large and covered a much wider range. For these data, the histogram was formed as a function of the velocity of the particles, computed as an integer percentage of the maximum velocity that the processor would admit, i.e.,

$$I_i = 100 \, \tau_1 \frac{n_i}{\Delta t_i} \tag{48}$$

where τ_1 is the minimum Doppler period and n_i is the number of fringes crossed by the i^{th} particle in time Δt_i.

The pruning was performed in two passes. First, data in any bin that contained only one count, and did not have neighboring bins with more than one count, were discarded. In the second pass, any data isolated from the main body of the histogram by at least one zero were also discarded. If, as a result of these two operations, more than 24 measurements out of the total of 1024 were rejected, the entire record was rejected. This scheme was preferred to the more usual one of rejecting data outside a certain number of standard deviations from the mean. By way of example, the few

counts in bin 40 of the histogram in Figure 19 would be discarded by this scheme.

The histograms which result from the data in the present investigations are illustrated in Figures 20 and 21. In these figures, the histograms at several locations through the boundary layer are superimposed on the mean-velocity profiles for that case. For both flows represented here, the histogram for the free-stream flow encompasses only four bins. Near the wall, the histogram is spread over more than forty bins.

B. Sampling Bias

The complexity of processing single particle laser-Doppler velocity data is compounded by the fact that the fluid velocity is sampled in a biased manner. This problem, first pointed out by McLaughlin and Tiederman (1973), is a consequence of the fact that the particle flux through the measurement volume, and the resulting measurement probability per unit time, is higher when the local fluid velocity is high than when it is low. The fact that the measurement probability is a function of the measured quantity gives rise to the sampling bias $\beta(\underline{u})$, where $\underline{u}$ is the three-dimensional velocity vector. Consequently, to compute the expectation value of a particular function of the measurements we must remove this bias, i.e.,

$$\langle f(\underline{u}) \rangle = \frac{\sum_i f(\underline{u}_i)\beta^{-1}(\underline{u}_i)}{\sum_i \beta^{-1}(\underline{u}_i)} \quad . \tag{49}$$

The dependence of the sampling bias function β on the local velocity vector $\underline{u}$, on the shape of the measurement volume, and on the minimum number of fringe crossings required by the processing electronics, has been derived

by Dimotakis (1976). For data recorded in the fixed-fringe mode, if the angle between the intersecting beams is small, the expression for $\beta(\underline{u})$ simplifies to

$$\beta(\underline{u};\epsilon) \simeq u_{\perp}(1 + u_{/\!/}^2/u_{\perp}^2)^{1/2}\,[1 - \epsilon^2(1 + u_{/\!/}^2/u_{\perp}^2)] \quad , \tag{50}$$

where $u_{\perp}$ is the velocity component perpendicular to the fringe planes, $u_{/\!/}$ is the velocity component parallel to the fringe planes and perpendicular to the beam bisector, and ϵ is the ratio n_{min}/n_T of the minimum number of fringe crossings required by the processor to the total number in the focal volume. Note that recording the flight time for a fixed number of fringes in fact requires that <u>at least</u> that many were crossed. Consequently, the fixed number of fringes is equal to n_{min} in the context in which ϵ was defined for Equation (50).

Evaluating $\beta(\underline{u};\epsilon)$ for the $u_{\perp}$ data in the boundary layer, which were acquired using the fixed-fringe mode ($0.6 \lesssim M_e \lesssim 2.2$), we note that $u_{/\!/}^2/u_{\perp}^2 = v^2/u^2 \ll 1$ so that, in this case,

$$\beta(\underline{u};\epsilon) \simeq u_{\perp}\cdot(1 - \epsilon^2) \tag{51}$$

or,

$$\beta(\underline{u};\epsilon) \propto u_{\perp} \quad . \tag{52}$$

In going from Equation (51) to Equation (52), an additional assumption has been made. Even though n_{min} is fixed by the signal processing electronics, the total number of fringes crossed, n_T, is unfortunately a complicated function of the particle size. This is a consequence of the fact that the amplitude levels V_0 and V_L are absolute. A large particle,

with a correspondingly large scattering cross-section, will yield a burst which is expected to result in more validated cycles. Thus, the ratio ϵ is a function of the particle size. In the context of Equation (49), the transition from Equation (51) to (52) is valid only if the local velocity vector is uncorrelated with particle size. This requirement will be satisfied if the particles track the flow.

With this proviso we then have from Equations (49) and (52), for the u_1 data in the fixed-fringe mode,

$$\langle f(\underline{u}) \rangle = \frac{\sum_i f(\underline{u}_i) u_{\perp_i}^{-1}}{\sum_i u_{\perp_i}^{-1}} \tag{53}$$

In particular, the mean velocity is given by

$$\langle u_\perp \rangle = \frac{N}{\sum_i u_{\perp_i}^{-1}} \tag{54}$$

where N is the total number of data points, as originally proposed by McLaughlin and Tiederman (1973). Similarly the mean square is given by,

$$\langle u_\perp^2 \rangle = \frac{\sum_i u_{\perp_i}}{\sum_i u_{\perp_i}^{-1}} \tag{55}$$

The mean-square fluctuations can then be computed by means of

$$\langle u'^2_\perp \rangle = \langle u_\perp^2 \rangle - \langle u_\perp \rangle^2 \tag{56}$$

$$\langle u'^{2}_{\perp} \rangle = \frac{\sum_{i} (u_{\perp i} - \langle u_{\perp} \rangle)^{2} \, u_{\perp i}^{-1}}{\sum_{i} u_{\perp i}^{-1}} \tag{57}$$

The latter form is preferable in avoiding finite precision problems in the computer, at the expense, however, of substantially more computing time.

In evaluating Equations (54) and (55), note that the i^{th} measured velocity component is given by Equation (47), or

$$u_{\perp i} = \frac{ns}{\tau_c} \left(\frac{1}{k_i + \frac{1}{2} + x} \right) \tag{58}$$

where n is equal to the number of fringes, s is the fringe spacing, τ_c is the clock period (10 nsec), k_i is the (integer) output of the flight time counter and x is a random variable representing the collective uncertainty in the determination of the flight time Δt and resulting from (i) the finite clock period τ_c, and (ii) the uncertainty with which the equal phase points are determined by the comparators from the signal burst as a result of finite signal-to-noise ratio. The 1/2 is added to k_i to remove the systematic truncation error of the digital counter.

Using Equations (54) and (55) and correcting for the finite variance of the random variable x, we have

$$\langle u_{\perp} \rangle_{fixed} = \left(\frac{ns}{\tau_c} \right) \frac{N}{J_{-1}} \quad , \tag{59}$$

and

$$\langle u_{\perp}^{2} \rangle_{fixed} \simeq \left(\frac{ns}{\tau_c} \right)^{2} \left(\frac{J_2 - \sigma^2 J_3}{J_{-1}} \right) \quad , \tag{60}$$

where

$$J_{\ell} \equiv \sum_{i} (k_i + \frac{1}{2})^{-\ell} \tag{61}$$

and

$$\sigma^2 \equiv \frac{\int x^2 p(x)dx}{\int p(x)dx} \tag{62}$$

is the variance of x.

Unfortunately, the situation is less well defined for the $\pm 45^{\circ}$ data recorded in the fixed-fringe mode. In that case, the two relevant velocities, $u_{\perp}$ and $u_{/\!/}$, are of the same order of magnitude. Nevertheless, since only one velocity component was measured at a time, we use Equation (52) for the bias and reduce the $\pm 45^{\circ}$ data using Equations (59) and (60). While this is clearly not correct, it is better than ignoring the bias altogether.

Note that the expression for the sampling bias β given by Equation (52) is not appropriate for data acquired in the free-fringe mode because this equation was derived using the assumption that the probability of measurement is determined by the fact that the particle has crossed at least the fixed number of fringes. In the free-fringe mode, the measurement of the number of fringes crossed and of the flight time in units of τ_c corresponds to a particle crossing of <u>exactly</u> n_i fringes. The probability for this event can be determined from Equation (50). Since $\beta\ (\underline{u};\ n_i/n_T)$ is proportional to the probability of crossing at least n_i fringes, i.e.,

$$\beta_{\text{fixed}}\ (\underline{u}; n_i/n_T) \propto \dot{p}\ \{n < n_i \,|\, \underline{u}\} \tag{63}$$

we have that

$$\dot{p}\{n = n_i \mid \underline{u}\} = \dot{p}\{n < n_i \mid \underline{u}\} - \dot{p}\{n < (n_i + 1) \mid \underline{u}\} \quad , \tag{64}$$

where $\dot{p}\{\ \}$ denotes the probability per unit time of observing the event in the braces. Consequently,

$$\beta_{free}(\underline{u}; n_i/n_T) \propto \beta_{fixed}(\underline{u}; n_i/n_T) - \beta_{fixed}[\underline{u}; (n_i + 1)/n_T] \quad , \tag{65}$$

$$\beta_{free}(\underline{u}; n_i/n_T) \propto u_\perp^{-2}(u_\perp^2 + u_{/\!/}^2)^{3/2}(n_i + 1/2) \tag{66}$$

where, in the context of Equation (49), the assumption has been made that the particle size is uncorrelated with the local velocity. In the context of Equation (49), note that

$$u_\perp \propto \frac{n_i}{\Delta t_i} \quad , \tag{67}$$

whereas

$$(u_\perp^2 + u_{/\!/}^2) \propto \frac{1}{\Delta t_i} \quad , \tag{68}$$

where Δt_i is the time of flight for the measured n_i fringes. Substituting these equations in Equation (66), we have

$$\beta_{free}^{-1}(\underline{u}; n_i/n_T) \propto \frac{(k_i + 1/2 + x)n_i^2}{n_i + 1/2} \quad , \tag{69}$$

where, as before, k_i is the integer output of the flight time counter and x is a random variable representing the uncertainty in the measurement of

the flight time. Using this bias function, we thus have

$$\langle u_\perp \rangle_{free} = \left(\frac{ns}{\tau_c}\right) \frac{K_{0,3}}{K_{-1,2}} \quad , \tag{70}$$

and

$$\langle u_\perp^2 \rangle_{free} = \left(\frac{ns}{\tau_c}\right)^2 \left(\frac{K_{1,4} - \sigma^2 K_{3,4}}{K_{-1,2}}\right) \quad , \tag{71}$$

where

$$K_{\ell,m} \equiv \sum_i \frac{n_i^m}{(k_i + \frac{1}{2})^\ell (n_i + \frac{1}{2})} \quad , \tag{72}$$

and σ^2 is the variance of x. Note that Equations (70) and (71) are equally valid for the 0^o data as for the $\pm 45^o$ data. The data recorded at $M_e \simeq 0.1$ in the free-fringe mode were analyzed using Equations (70) and (71). In order to compare them to the previous data, Equations (54) and (55) were also used, which in this case reduce to

$$\langle u_\perp \rangle = \left(\frac{s}{\tau_c}\right) \frac{L_{0,1}}{L_{-1,-1}} \quad , \tag{73}$$

and

$$\langle u_\perp^2 \rangle = \left(\frac{s}{\tau_c}\right)^2 \left(\frac{L_{1,1} - \sigma^2 L_{3,1}}{L_{-1,-1}}\right) \quad , \tag{74}$$

where

$$L_{\ell,m} = \sum_i \frac{n_i^m}{(k_i + \frac{1}{2})^\ell} \quad . \tag{75}$$

Note also that Equation (69) for the sampling bias in the free-fringe mode is in disagreement with the results of Hoesel and Rodi (1977) and Buchhave, George and Lumley (1979), who claim that $\beta_{free}^{-1} \propto \Delta t_i \propto (k_i \pm \frac{1}{2})$. If that were true, Equations (59) and (60) would be valid for the free-fringe mode as well, with the three summations as defined in Equation (61).

The variance σ^2 of x was estimated from the mean-square fluctuations in the free stream where $\langle u'^2 \rangle \simeq 0$.

The results of this analysis have been applied to the data obtained in these experiments. The bias correction is most important in the region near the wall, where the fluctuation levels are highest. These calculations indicate at most a 2% correction for the low-speed flow data in this region, and a 3.3% correction for the high-speed flow data.

VII. Results and Discussion

A. Data Reduction

Following the computation of the proper statistical averages, the data were reduced to a form appropriate for boundary layer flows by utilizing the scheme outlined in Part I of this report by Collins, Coles and Hicks (1978). For this purpose, the Van Driest (1955) scaled mean streamwise velocity data were fitted to the law of the wall and the law of the wake using a three-parameter nonlinear least-squares fit with a single constraint equation based on the local friction law. The profile parameters u_τ, Π and δ, determined by this analysis, were then used to infer both the distribution of shear stress, and of the normal velocity, from the data by an integration of the equations for the conservation of mass and momentum from the wall to the free stream, using the formulation by Spalding (1961) to describe the flow in the viscous sublayer. The details of these computations are given in Part I.

One significant difference between the present LDV data and the data obtained using standard Pitot instrumentation (cf. Part I) is the ability of the Pitot to obtain valid data in the region adjacent to the wall. Because of noise considerations, the present data are limited to a distance of approximately one focal-volume diameter from the wall. This fact requires that the boundary-layer scale parameters δ^* and θ be computed directly from the law of the wall and the law of the wake representations rather than from a direct integration of the data, as in the results discussed in Part I.

The scale parameters are defined as

$$\delta^* = \int_o^\delta \left[1 - \frac{\rho u}{\rho_e u_e}\right] dy \quad , \tag{76}$$

and

$$\theta = \int_o^\delta \frac{\rho u}{\rho_e u_e} \left[1 - \frac{u}{u_e}\right] dy \tag{77}$$

In terms of the Van Driest (1955) scaled velocity U,

$$\frac{\rho u}{\rho_e u_e} = \frac{1}{m} \frac{T_e}{T_w} \frac{\sin U}{\cos^2 U} \quad , \tag{78}$$

and

$$\frac{\rho u^2}{\rho_e u_e^2} = \frac{1}{m^2} \frac{T_e}{T_w} \frac{\sin^2 U}{\cos^2 U} \quad , \tag{79}$$

where

$$m = \left(\frac{T_w - T_e}{T_w}\right)^{1/2} \quad , \tag{80}$$

and U is defined by the Van Driest scaling

$$m \frac{u}{u_e} = \sin U \quad . \tag{81}$$

Thus,

$$\delta^* = \delta - \frac{1}{m} \frac{T_e}{T_w} \int_o^\delta \frac{\sin U}{\cos^2 U} \, dy \quad , \tag{82}$$

and

$$\theta = \frac{1}{m} \frac{T_e}{T_w} \int_o^\delta \frac{\sin U}{\cos^2 U} \, dy - \frac{1}{m^2} \frac{T_e}{T_w} \int_o^\delta \frac{\sin^2 U}{\cos^2 U} \, dy \quad . \tag{83}$$

The integrals involved in these expressions were evaluated in terms of the integrals P and Q defined in Part I. These integrals are functions only of the mean-velocity profile parameters u_τ, Π and δ, and are evaluated in terms of the Spalding formulation for the boundary layer.

As a result of the differences in the computational procedure for the scale parameters δ^* and θ, these quantities differ slightly from those computed for the identical flows given in Part I of this work. Corrections for these discrepancies have been included where comparisons are made to the previous work.

B. Streamwise Mean-Velocity Profiles

A comparison between the mean-velocity profiles obtained in the present experiments and those obtained from the Pitot data of Part I is given in Figures 22 and 23. In order to make a consistent comparison, the Pitot data from Part I have been replotted using the integral scale θ obtained from the LDV experiments. At high Mach numbers, the results exhibit a small discrepancy between the LDV and the Pitot data, with the LDV data exhibiting lower mean velocities near the wall. The cause of this discrepancy is not clear at this writing, nor is it clear which measurement is the more reliable. The low-speed flow mean-velocity profiles have been computed using both the exact bias correction, according to Equation (70) and using the harmonic mean according to Equation (59). The differences are small as are the

differences between these results and the results of the mean value of these data without any bias correction. The comparisons have not been plotted here. The agreement between the LDV data and the Pitot data is excellent for the low-speed results.

The data obtained from the present experiments have been plotted in coordinates appropriate to the law of the wall in Figures 24 and 25. The solid line associated with each data set has been computed using the formulation by Spalding (1961), and illustrates the fit obtained in the computation of u_τ, Π and δ. The high-speed flow results shown in these figures illustrate the problem of obtaining measurements near the wall. These data exhibit a departure from the computed profile because of noise which occurs when the focal volume intercepts the wall. This fact required that the data included in the least-squares fit be limited to $y^+ \geq 200$ for these data, as was the case for the Pitot data reported in Part I.

The profile parameters u_τ and δ computed from the least-squares procedure agree closely with those parameters computed from the Pitot data for the same flows. The computations of the wake parameter Π, however, are considerably higher in every case. The self-consistency of the LDV results indicates that this discrepancy is probably not the consequence of data reduction errors.

C. Streamwise Velocity Fluctuations

The fluctuations of the streamwise velocity component, normalized by the free-stream velocity, are shown in Figures 26 and 27 as a function of the normal coordinate. These results are compared to the distribution of the u' fluctuations obtained at low speeds by Klebanoff (1954) in flow at constant pressure, represented by the solid squares in these figures. For

these comparisons, the normal coordinate for the data by Klebanoff have been scaled with the boundary-layer scale obtained in the present experiments.

The error bars in each of the subsequent figures have been computed as the standard deviation of the ensemble of records used in computing the mean values. In each case, a few data points for which the error bars exceed the mean value have been excluded. From these results, it is clear that, near the free-stream, the velocity fluctuations are properly computed from the LDV data. As the wall is approached, the deviations between the present results and those of Kelbanoff are within the confidence limits in the present data.

It can be concluded from these data that, within the error in the present experiments, no measurable effects of compressibility have been found on the mean-square velocity fluctuations. The data for Mach numbers up to 2.2 are adequately represented by the data of Klebanoff. The differences exhibited in these figures between the high-speed flow data and the low-speed flow data arise from the differences in the boundary-layer Reynolds number, Re_θ. These results confirm Morkovin's (1961) hypothesis that there is no essential difference in the dynamic behavior of the boundary layer at constant pressure for Mach numbers up to 4 or 5.

D. Reynolds Stress Profiles

The distribution of Reynolds stress, computed as $-\rho\overline{u'v'}$, is shown in Figures 28 and 29 for the data of these experiments. In order to compare the Reynolds stress deduced from the experimental data with the expected distribution through the boundary layer, a second computation based on the integral formulation outlined in Part I is displayed as the solid curve in each figure. The results from the integral formulation coincide with the

results obtained using the Pitot data, with minor differences arising from the difference in the computed value of the wake parameter Π.

For comparison with the expected behavior at low speeds, the data of Klebanoff (1954) has been included in these figures as the dark squares on each figure. The agreement between the integral formulation and the data of Klebanoff indicates that the integral formulation, based on the mean-velocity data, yields the expected distribution for the total shear stress.

The dominant feature of the results for the distribution of the Reynolds stress, as measured by the laser-Doppler technique, is the departure of the measured Reynolds stress from the results of the integral computation in the region $y/\theta \lesssim 3$. This departure represents a major error in these measurements and may indicate a fundamental limitation on the applicability of the laser-Doppler technique in flows of this type.

Several conclusions can be reached from these data. The anomaly represented by the departure of the Reynolds stress from the expected value near the wall has been reported previously by Johnson and Rose (1973), by Yanta and Lee (1974), and by Abbiss (1976). An explanation of this phenomenon by Sandborn (1974) assumed that the phenomenon is related to the contributions of density fluctuations to the Reynolds stress. That this assumption is incorrect is clear from the present data. The observed phenomenon is not Mach number dependent and hence is not an effect of compressibility. These data also indicate that the discrepancy in the Reynolds stress is not associated with particle lag at the position of measurement, because for this to be the case the results of Equation (13) require that the lag occur at increasing distances from the wall with increasing free-stream velocity. In addition, the agreement obtained in the distribution

of the mean-square velocity fluctuations indicates that the particles follow the flow locally throughout the boundary layer.

Similar distributions for the Reynolds stress, measured using hot-wire anemometer techniques by Laderman (1978), have recently been shown to agree with the present results given by the integral distributions shown by the solid curves in Figures 28 and 29.

These results again confirm Morkovin's hypothesis (1961) and refute the hypothesis by Sandborn (1974) that density fluctuations may be responsible for major changes in the distribution of Reynolds stress at high speeds. Similar conclusions were expressed in Part I, based on the results of the Pitot measurements of the mean-velocity profiles.

E. The Problem of the Normal Velocity

The results for the distribution of normal velocity are illustrated in Figure 30 for the high-speed flow at low Reynolds number. In this figure, the solid line is the result for the correct distribution of v/u, computed from the integral representation of the data outlined by Collins, Coles and Hicks (1978), using the boundary-layer parameters u_T, Π and δ derived from the least-squares analysis.

The errors in estimating the normal velocity from the present data are substantial in every case. The principal feature of the data is that the normal velocity is large and negative at the wall, increasing sharply in magnitude as the wall is approached. The disparity between the large negative value and the error bars indicates that the particles are being convected toward the wall in this region. In the free stream, the velocity is positive in most cases, but with a magnitude that is larger than the correct free-stream value as represented by the integral formulation.

These data illustrate the difficulty in accurately representing the normal velocity. This difficulty arises as a consequence of the fact that any small misalignment of the optics will result in substantial errors in the computed value of the normal velocity, which has a maximum value

$$(v/u) \lesssim \frac{HC_f}{2} \quad , \tag{84}$$

where $H = \delta^*/\theta$ is the boundary layer form parameter. In addition, because of the non-uniform particle distributions, the normal velocity components of both the flow near the wall and the flow in the vicinity of the boundary-layer edge are improperly represented.

The fluctuations in the normal velocity are represented for these same data in Figure 31. These data have approximately the value of the data of Klebanoff (1954) for incompressible flow, represented by the solid squares in the figure. However, in light of the difficulties in measuring the normal velocity, this agreement is fortuitous. The magnitude of the error bars for these data are approximately one-half of the magnitude of the data, and indicate a low degree of confidence in the results.

VIII. Conclusions

The present experiments lead to a number of conclusions regarding the applicability of the laser-Doppler technique to the study of boundary-layer flows. The results presented for the behavior of the streamwise velocity components indicate the importance of including in the analysis of the raw data an adequate technique for pruning the initial histograms in order to remove errors in the data introduced by noise. These results further indicate the importance of including proper statistical averaging in the analysis in

order to account for the bias introduced by sampling. In addition, the effects of a finite clock period and noise have been shown to be important in the proper determination of the streamwise velocity fluctuations, u', near the boundary-layer edge. When these effects are properly included in the data analysis, a direct comparison between the present laser-Doppler measurements and measurements in the same flows, presented in Part I of this work, indicates good agreement for the streamwise velocity components u and u'. The present results, when properly scaled to account for compressibility using the ideas of Van Driest (1955), are also shown to agree with the low-speed data presented by Klebanoff (1954). This observation further corroborates the conclusions expressed in Part I of this work regarding the proper role of compressibility in determining the behavior of the mean velocity, and confirms Morkovin's hypothesis (1961) regarding the role of density fluctuations in the boundary layer at constant pressure.

The present measurements of the Reynolds stress, $-\rho\overline{u'v'}$, and for the normal velocity, v, are in substantial disagreement with the expected results derived from the mean flow. These observations seem to indicate a fundamental difficulty with the application of the laser-Doppler technique as implemented in these experiments to the measurement of the detailed structure of flows in the vicinity of a wall. The measured Reynolds stress profiles, $-\rho\overline{u'v'}$, deviate from the expected behavior for $y/\theta \lesssim 3$, indicating an error in the measurement for the $\overline{u'v'}$ correlation in the region adjacent to the wall. This error arises because of the strong correlation between the normal velocity component and the particle number density that occurs as a result of the depletion of particles near the wall. These results indicate that

the flow inside the viscous sublayer is such that a particle that enters the sublayer has a very low probability of leaving. The scaling law for particle behavior in a turbulent boundary layer (cf. Equation (13)) is not applicable in the viscous sublayer. A particle which enters the viscous sublayer is subjected to the very high Lagrangian frequencies which occur in the motion of the longitudinal vorticies, whose transverse extent is approximately $\frac{20\nu}{u_\tau}$, and lags the flow in this region. As a consequence, a fluid element coming <u>from</u> the wall is less likely to carry particles than a fluid element moving <u>toward</u> the wall. This results in an under-representation of the positive component of the normal velocity, v, in the region near the wall, resulting in a negative value for the measured component normal to the wall.

This under-representation of the motion near the wall also results in a lower measured value for the Reynolds stress, $-\rho\overline{u'v'}$, than would be expected by an analysis based on the mean flow as described in Part I, since the upswelling of fluid from the wall is associated with a lower streamwise velocity. This bursting motion has been observed by Blackwelder and Kaplan (1976) to be intermittent and quite violent, and is held to be responsible for a large fraction of the total stress near the wall $\left(\frac{yu_\tau}{\nu} \lesssim 100\right)$. The particle transport to the wall via the viscous sublayer is so effective, even at the lower velocities of the Merrill wind tunnel experiments, that the wall appears as an infinite sink for particles.

We conclude from these observations that the measured disparity between the Reynolds stress, $-\rho\overline{u'v'}$, and the total stress, as defined by the integration of the mean flow, arise not as a consequence of compressibility, as suggested by Sandborn (1974), but as a consequence of particle depletion which is unique to boundary layers in air. This is a fundamental limitation

of the techniques for particle seeding which must be solved if this technique is to be useful for detailed measurements near the wall. For free-shear flows, because of the absence of the wall, this problem does not arise, and the laser-Doppler technique will give an accurate representation of the mean and fluctuating velocity components and their correlations.

References

1. Abbiss, J. B. 1976 Development of photon correlation anemometry for application to supersonic flow. AGARD CP-193, "Applications of Non-Intrusive Instrumentation in Fluid Flow Research," 11.1 - 11.11.

2. Blackwelder, R. F. and Kaplan, R. E. 1976 On the wall structure of the turbulent boundary layer. J. Fluid Mech. 76, 89-112.

3. Buchhave, P., George, W. K, Lumley, J. L. 1979 The measurement of turbulence with the laser-Doppler anemometer. Ann. Rev. Fluid Mech. 11, 443-503, 1979.

4. Born, M. and Wolf, E. 1975 Principles of optics. Pergamon Press, New York, p. 633 ff.

5. Cantwell, B. 1978 Private communication.

6. Coles, D. E. 1968 The young person's guide to the data. Proc. 1968 AFOSR-IFP-Stanford Conf., "Computation of Turbulent Boundary Layers," Vol. II (D. Coles and E. Hirst, eds.), 1-45.

7. Collins, D. J., Coles, D. E. and Hicks, J. W. 1978 Measurements in the turbulent boundary layer at constant pressure in subsonic and supersonic flow. Part I. Mean flow. AEDC-TR-78-21.

8. Dimotakis, P. E. 1976 Single scattering particle laser-Doppler measurements of turbulence. AGARD CP-193, "Applications of Non-Intrusive Instrumentation in Fluid Flow Research," 10.1 - 10.14.

9. Dimotakis, P. E. and Brown, G. L. 1975 Large structure dynamics and entrainment in the mixing layer at high Reynolds number. Project Squid Tech. Rept. CIT-7-PU.

10. Dimotakis, P. E. and Lang, D. B. 1977 Signal responsive burst period timer and counter for laser-Doppler velocimetry and the like. U.S. Patent 4,051,433 (September 27, 1977).

11. Hoesel, W. and Rodi, W. 1977 New biasing elimination method for laser-Doppler velocimeter counter processing. Rev. Sci. Instrum. 48(7), 910-919.

12. Johnson, D. A. and Rose, W. C. 1973 Measurement of turbulence transport properties in a supersonic boundary-layer flow using laser velocimeter and hot-wire anemometer techniques. AIAA Paper 73-1045; see also AIAA J. 13, 512-515, 1975.

13. von Kármán, T. 1930 Mechanische ahnlichkeit und turbulenz. Proceedings 3rd International Congress for Applied Mechanics, Vol. 1, pp. 85-92.

14. Klebanoff, P. S. 1954 Characteristics of turbulence in a boundary layer with zero pressure gradient. NACA TN 3178; also TR 1247, 1955.

15. Laderman, A. J. 1978 Effects of Mach number and heat transfer on Reynolds shear stresses in compressible boundary layers. Aeronutronic Publication No. U-6412.

16. McLaughlin, D. K. and Tiederman, W. G. 1973 Biasing correction for individual realization of laser anemometer measurements in turbulent flows. Phys. Fluids 16, 2082-2088.

17. Morkovin, M. V. 1961 Effects of compressibility on turbulent flows. Proc. Colloq. Mechanique de la Turbulence, CNRS (1962), 367-380. (Proc. reprinted as Mechanics of Turbulence, Gordon & Breach 1964).

18. Perry, A. E. and Abell, C. J. 1975 Scaling laws for pipe flow turbulence. J. Fluid Mech. 67, 257-271.

19. Perry, A. E. and Abell, C. J. 1977 Asymptotic similarity of turbulence structures in smooth- and rough-walled pipes. J. Fluid Mech. 79(4), 785-799.

20. Prandtl, L. 1942 Z. Angew. Math. Mech. 22, 241-243, 1942.

21. Sandborn, V. A. 1974 A review of turbulence measurements in compressible flow. NASA TM X-62337.

22. Spalding, D. B. 1961 A single formula for the "law of the wall". Trans. ASME 28E (J. Appl. Mech.), 455-457.

23. Van Driest, E. R. 1955 The turbulent boundary layer with variable Prandtl number. "50 Jahre Grenzschichtforschung" (H. Görtler and W. Tollmien, eds.), Vieweg, Braunschweig, 257-271; see also The problem of aerodynamic heating, Aeron. Eng. Rev., Oct. 1956, 26-41.

24. Yanta, W. J. and Lee, R. E. 1974 Determination of turbulence transport properties with laser-Doppler velocimeter and conventional time-averaged mean flow measurements at Mach 3. AIAA Paper 74-575; see also AIAA J. 14, 725-729, 1976.

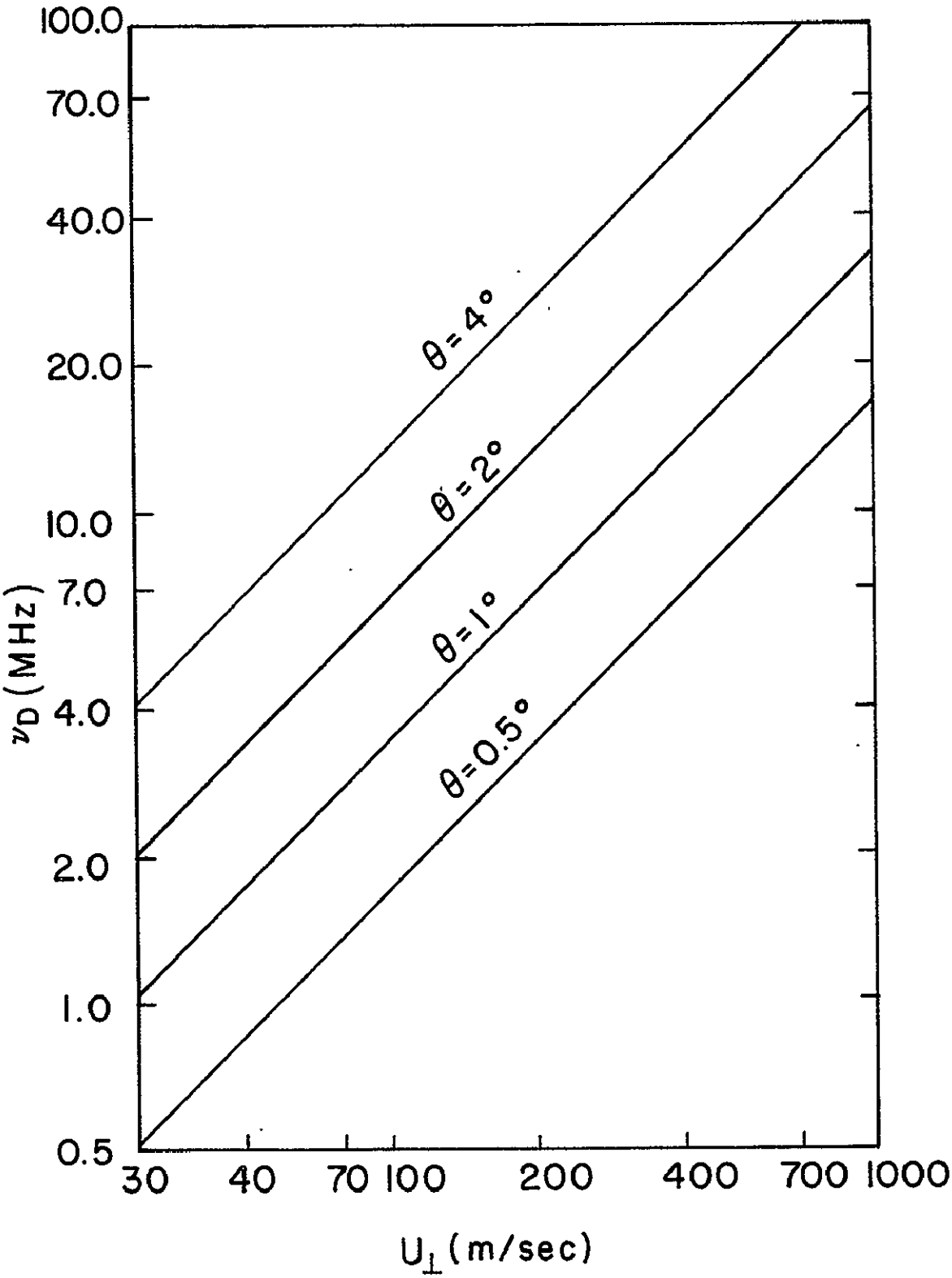

Figure 1. The Doppler frequency as a function of flow velocity.

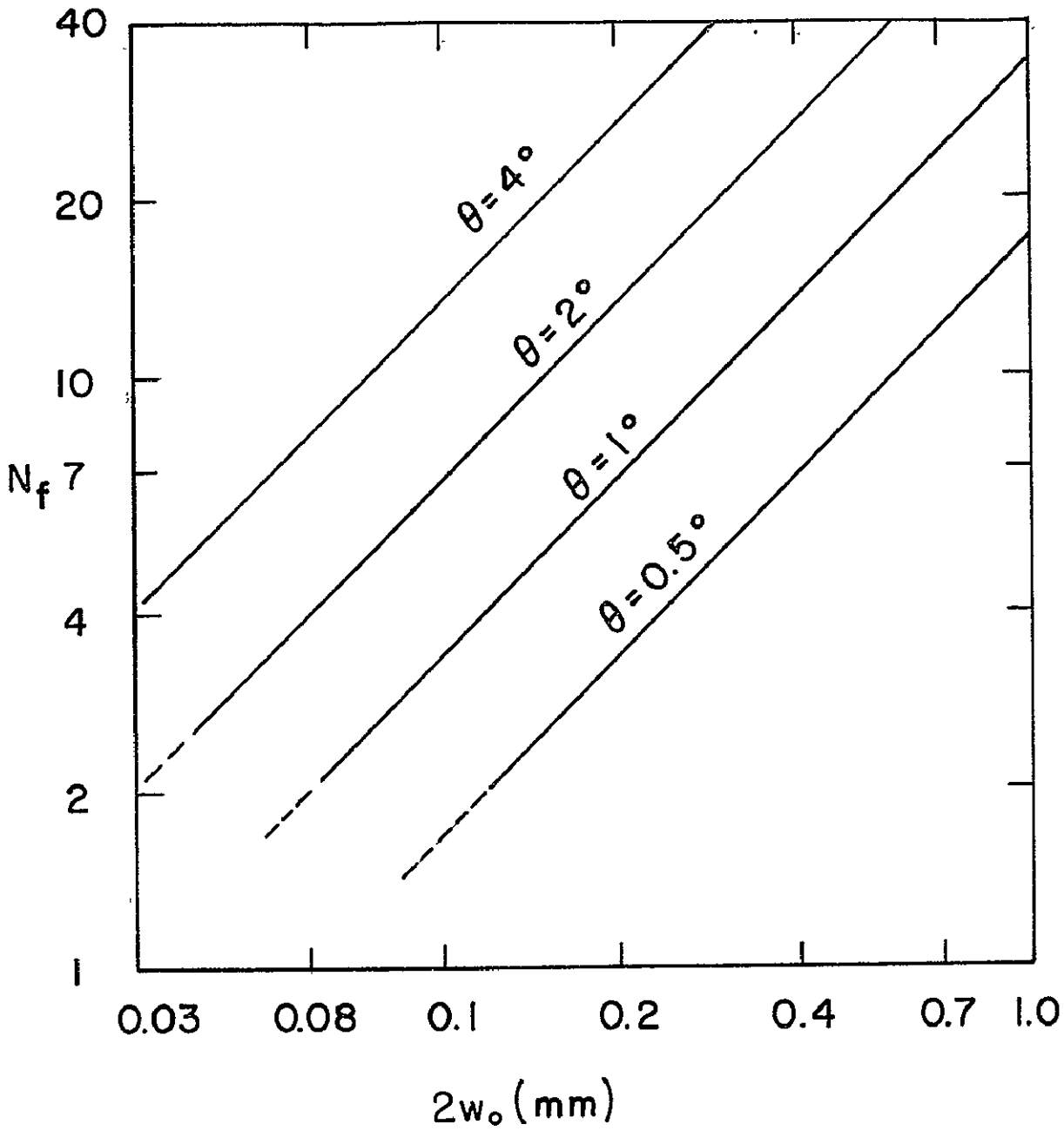

Figure 2. The number of fringes in the focal volume as a function of the focal volume diameter.

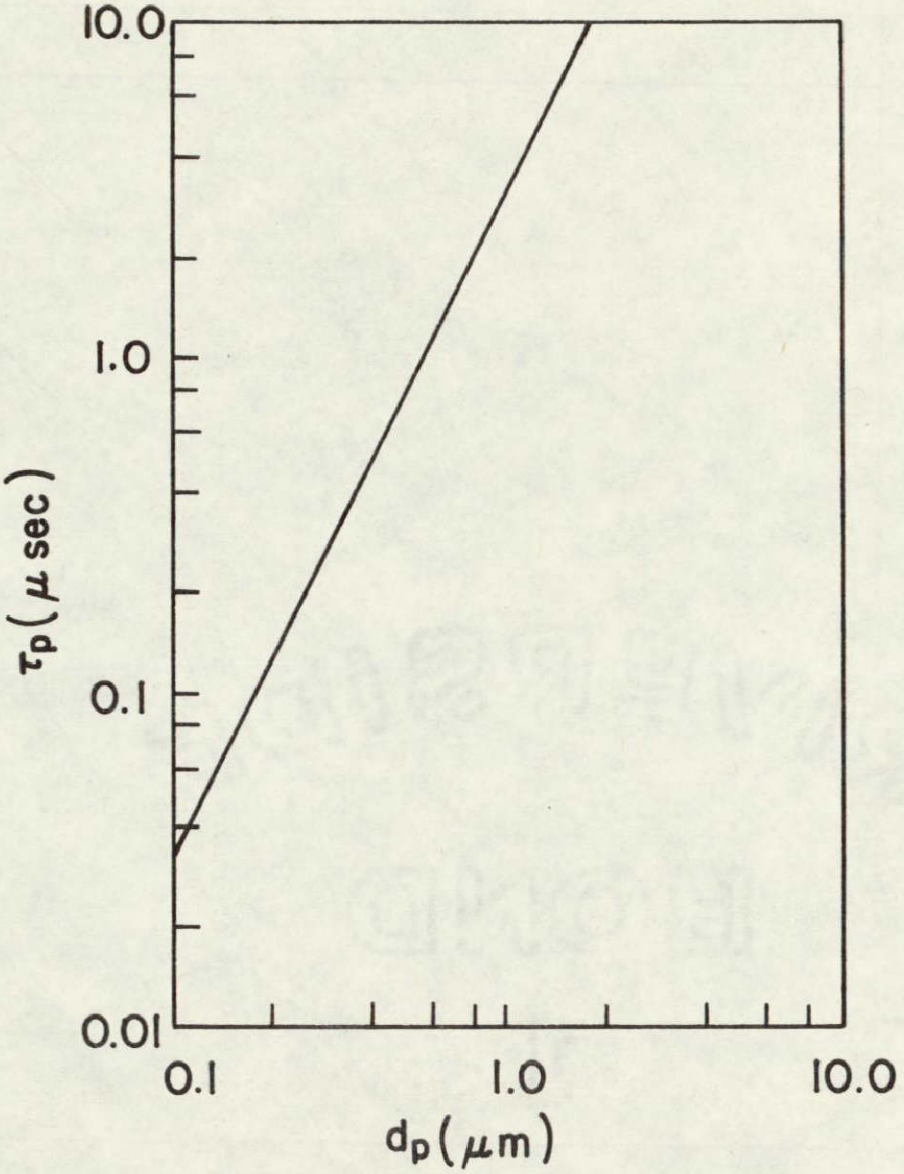

Figure 3. The particle response time as a function of particle diameter for di-butyl phthalate particles in air.

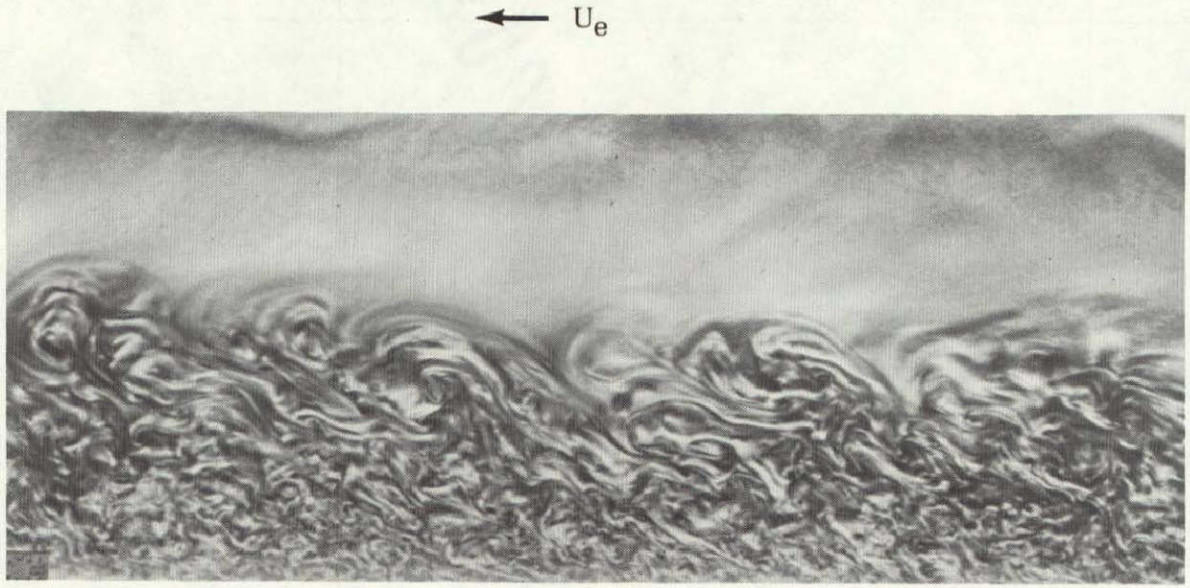

Figure 4. The structure of the turbulent boundary layer as visualized by the use of aluminum flakes in water; photograph courtesy of Brian Cantwell, Caltech (1978).

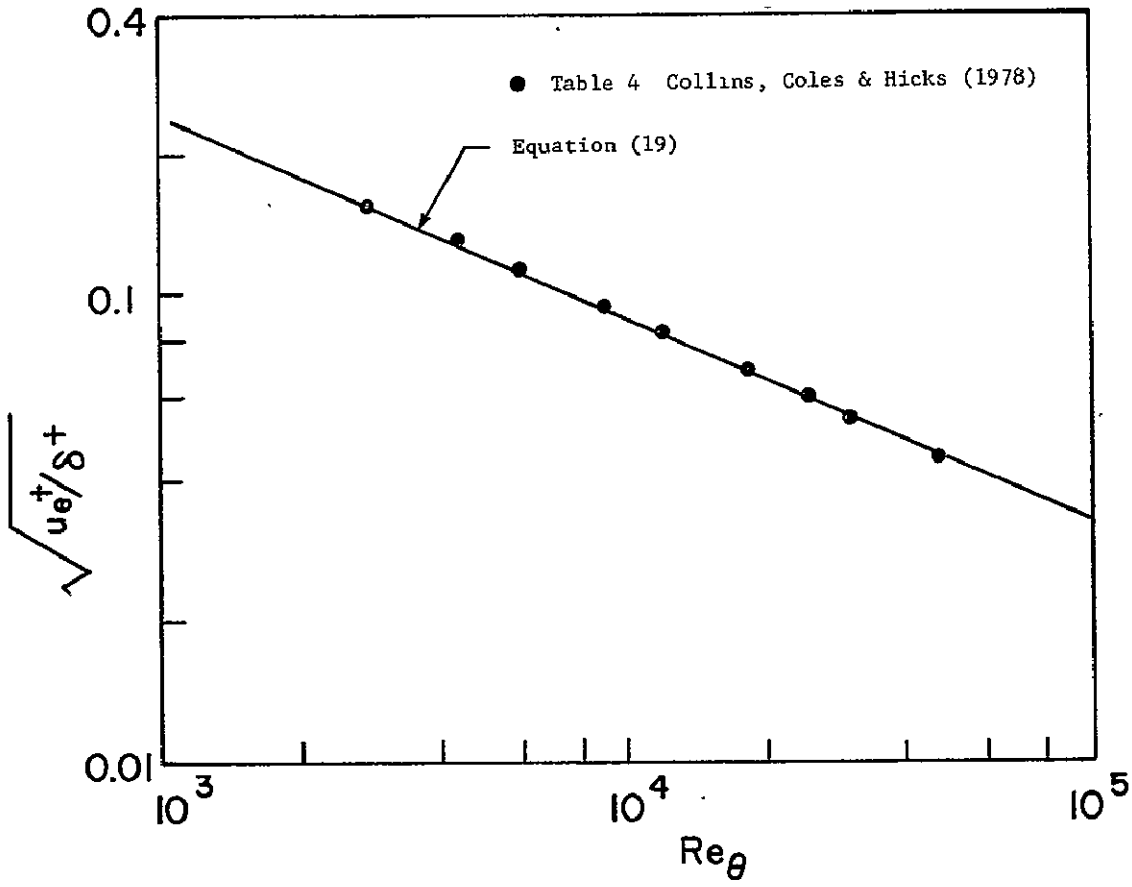

Figure 5. The ratio of the boundary-layer edge velocity to the boundary-layer thickness in wall coordinates as a function of Re_θ.

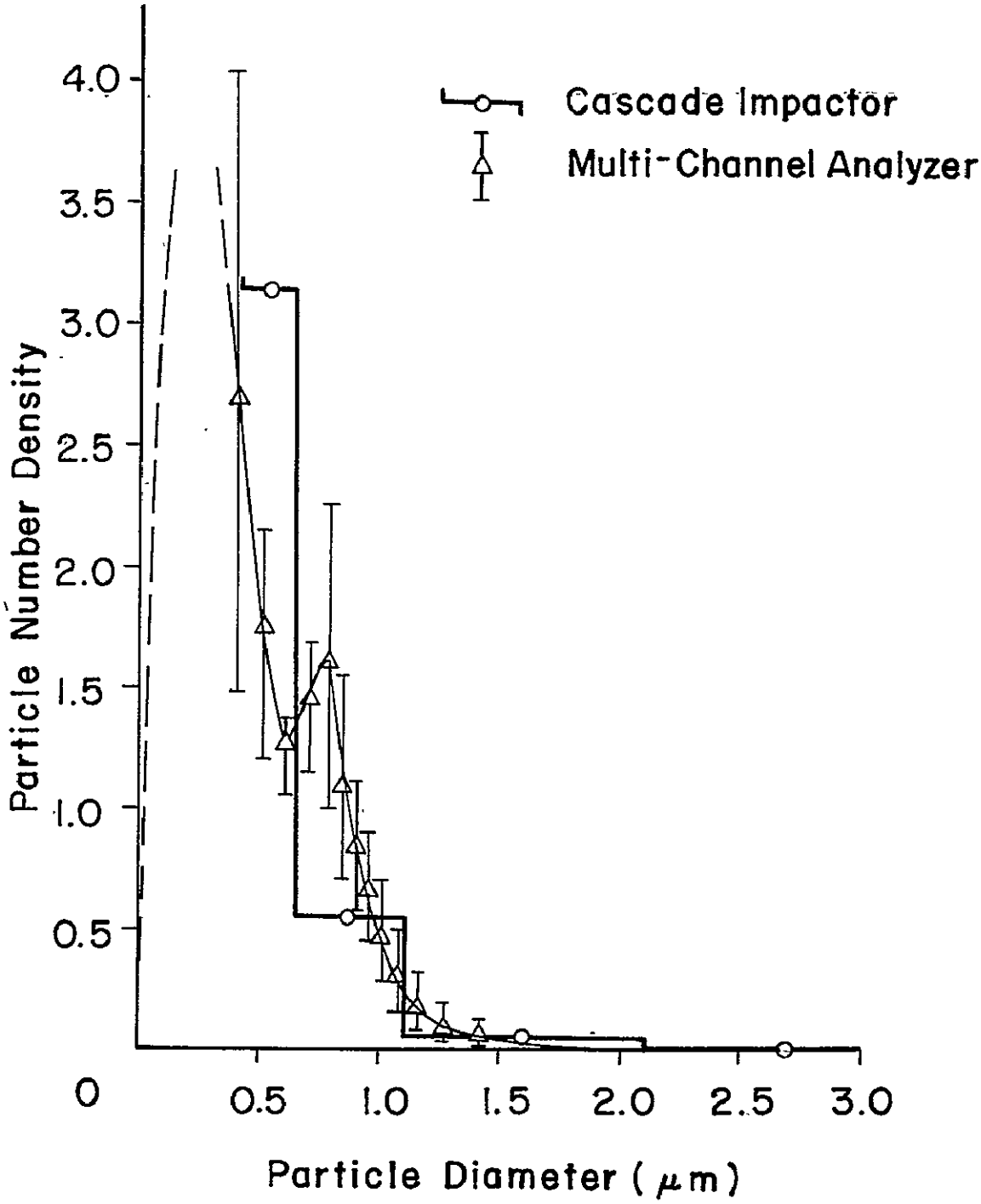

Figure 6. The particle size distribution.

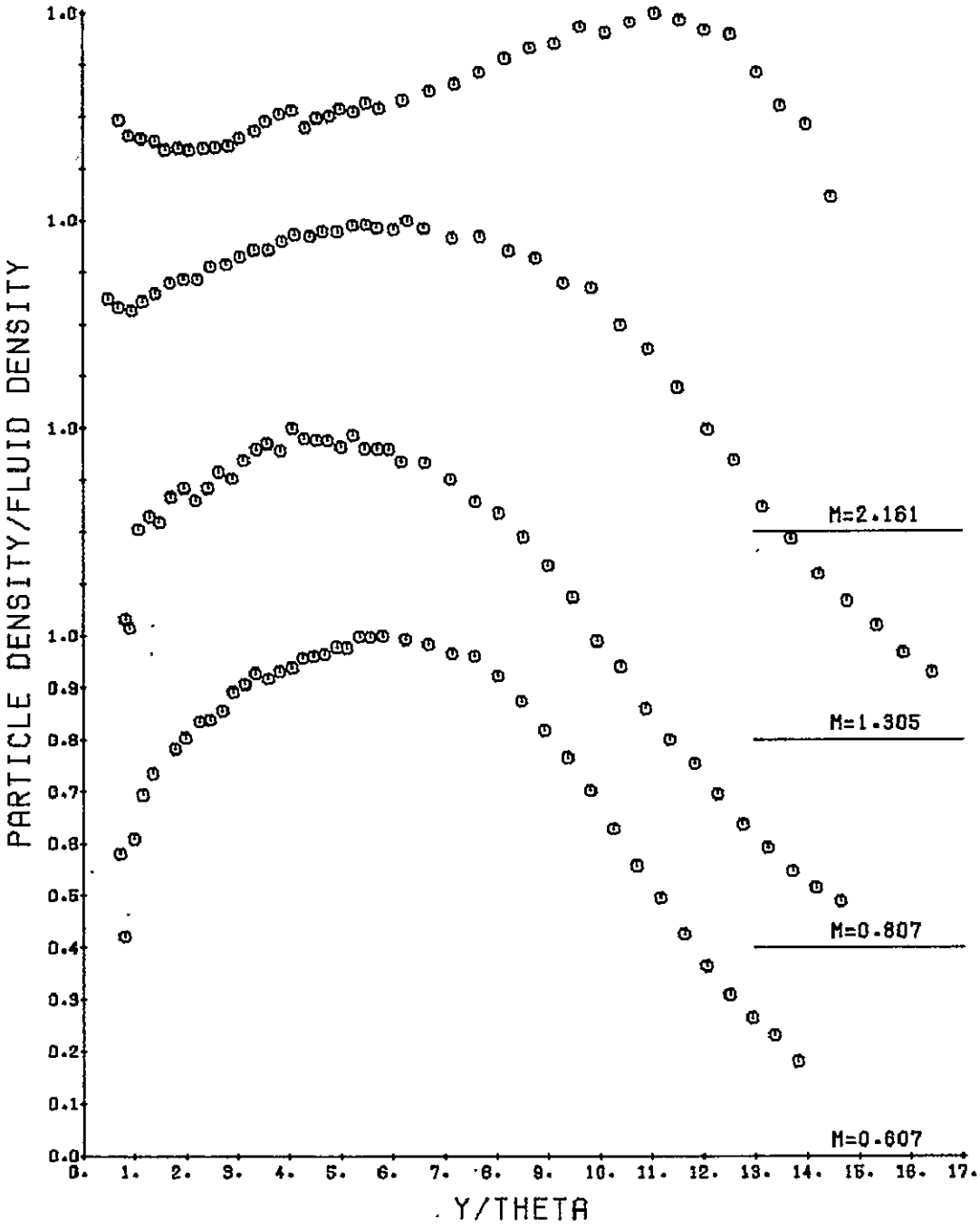

Figure 7. The distribution of particle number density, $Re_\theta \approx 23{,}000$.

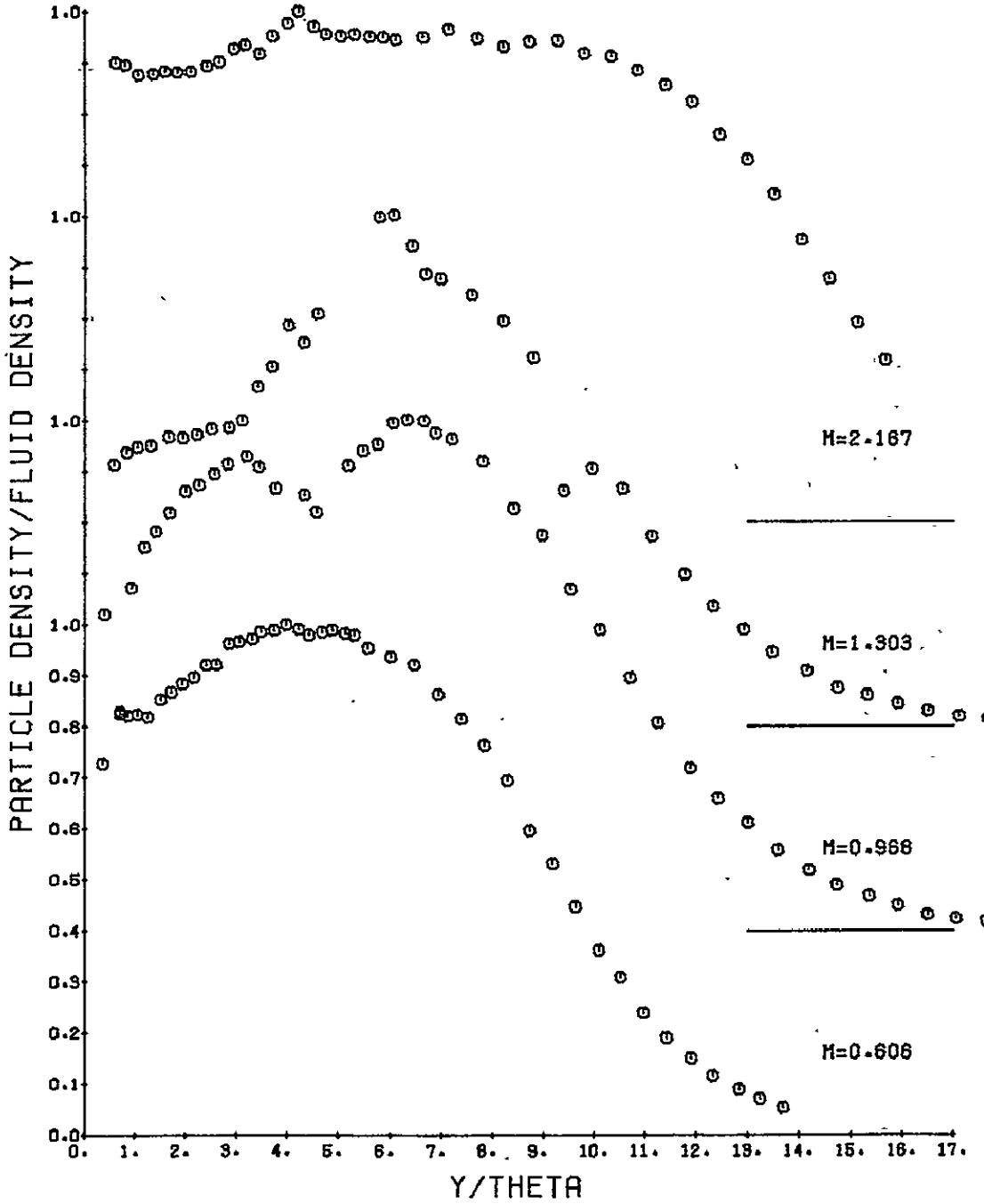

Figure 8. The distribution of particle number density, $Re_\theta \simeq 40{,}000$.

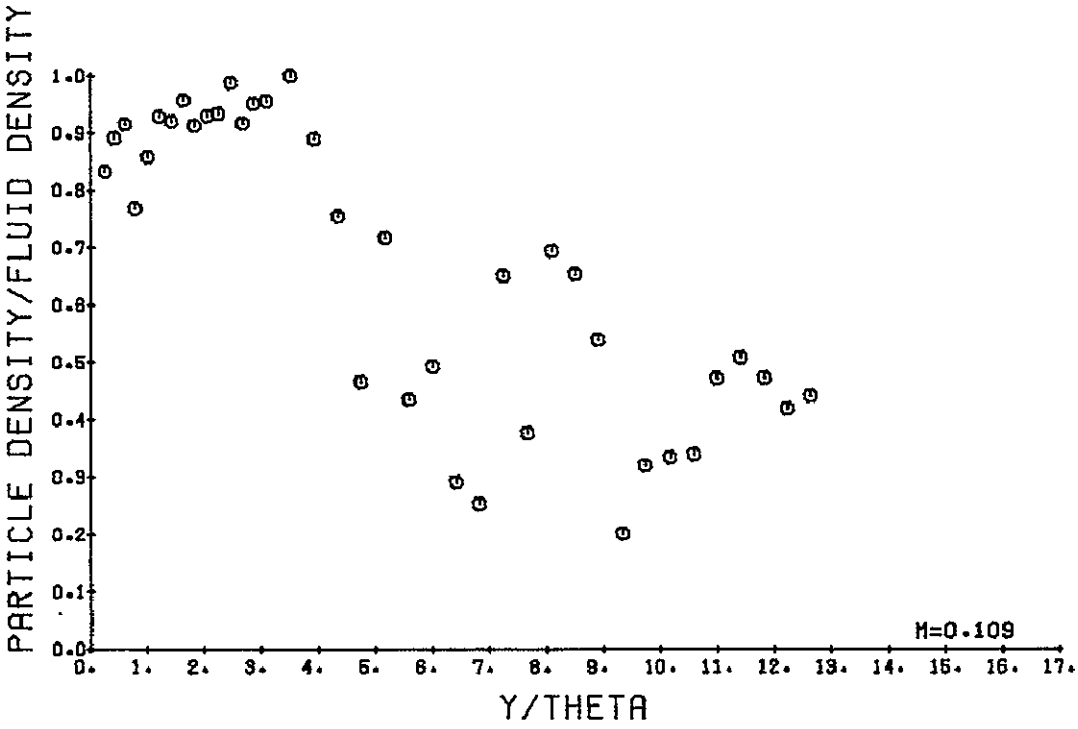

Figure 9. The distribution of particle number density, $Re_\theta \approx 6{,}900$.

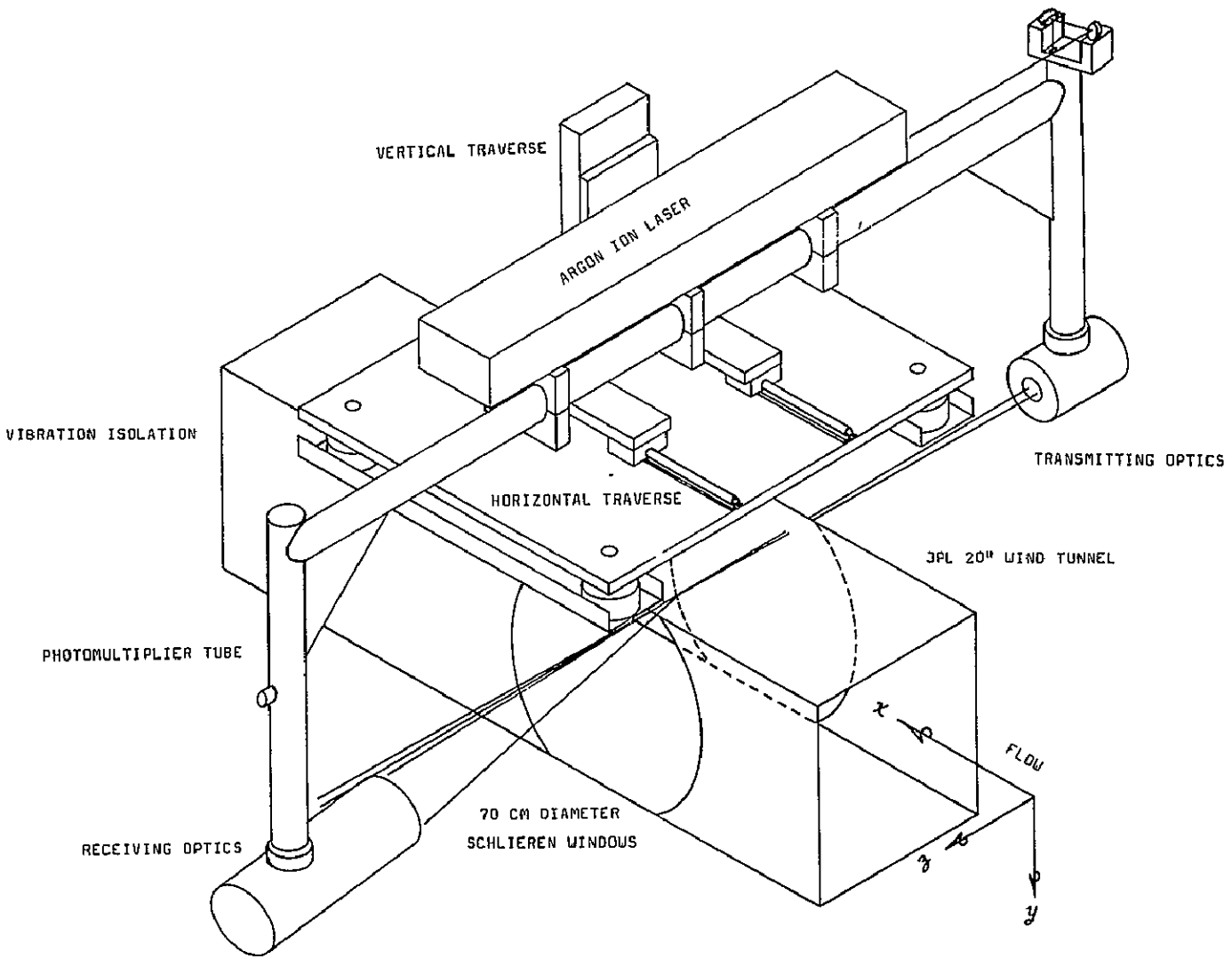

Figure 10. High-speed laser-Doppler velocimeter.

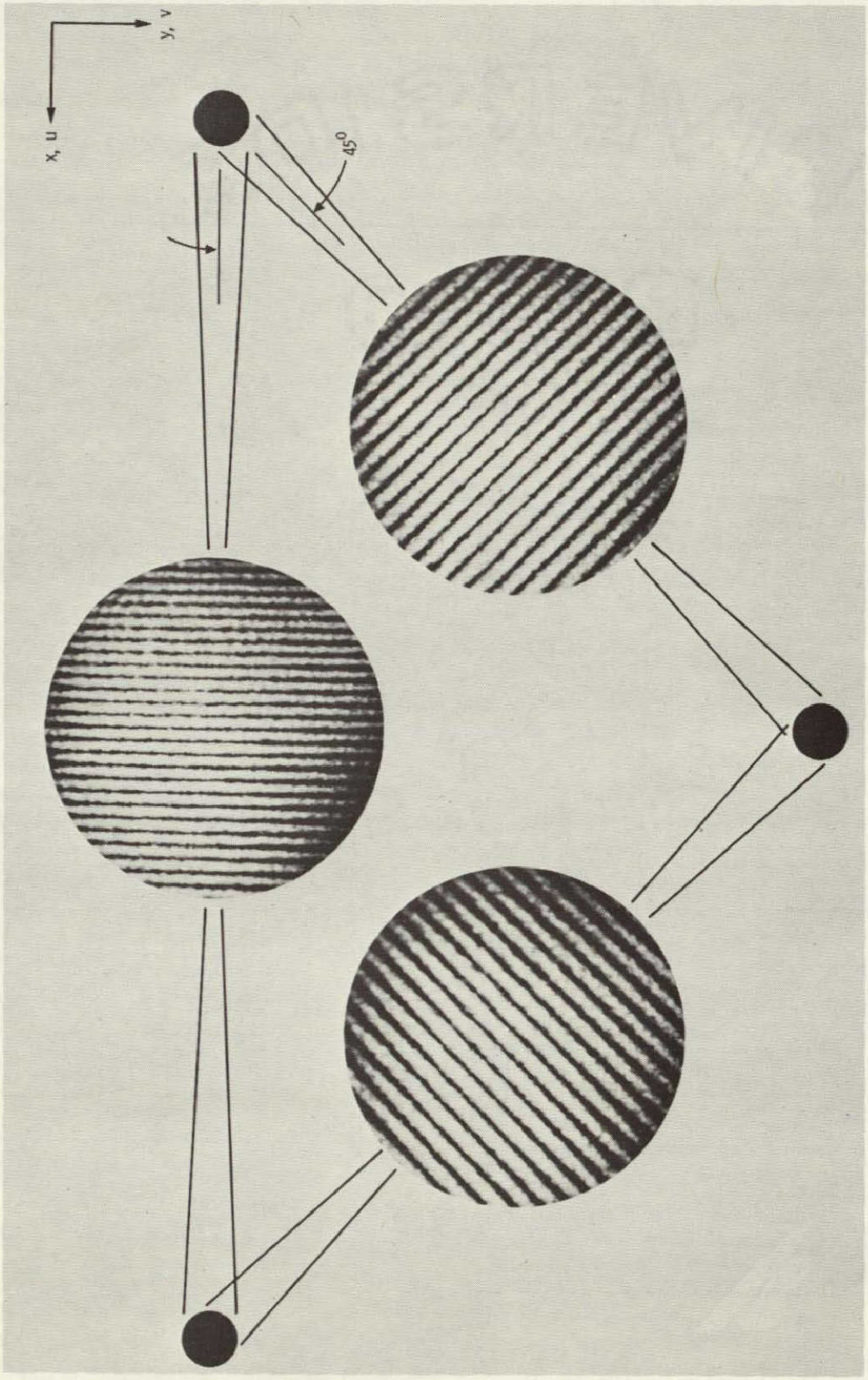

Figure 11. Optical geometry and fringe patterns for laser-Doppler anemometer.

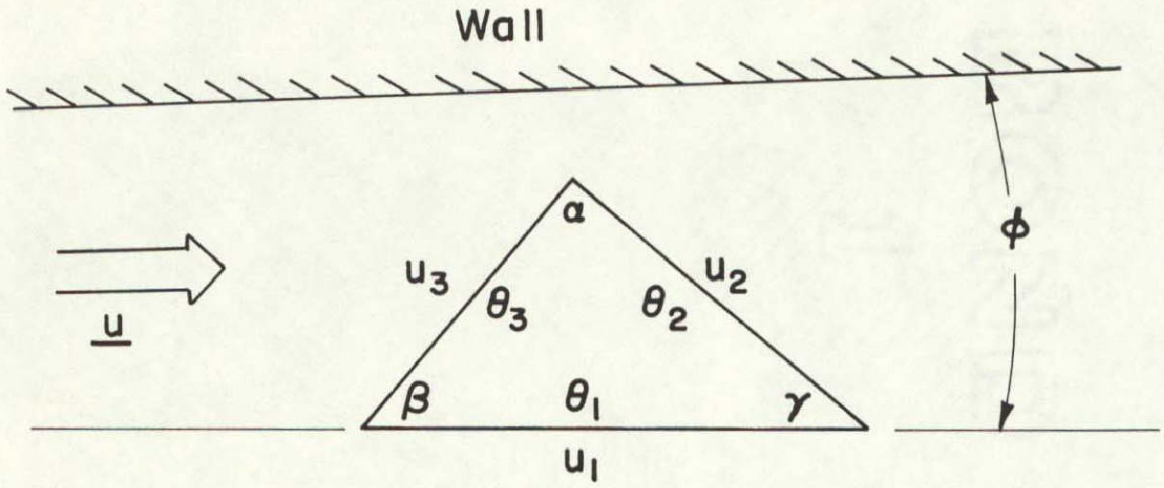

Figure 12. The optical geometry relative to the wall.

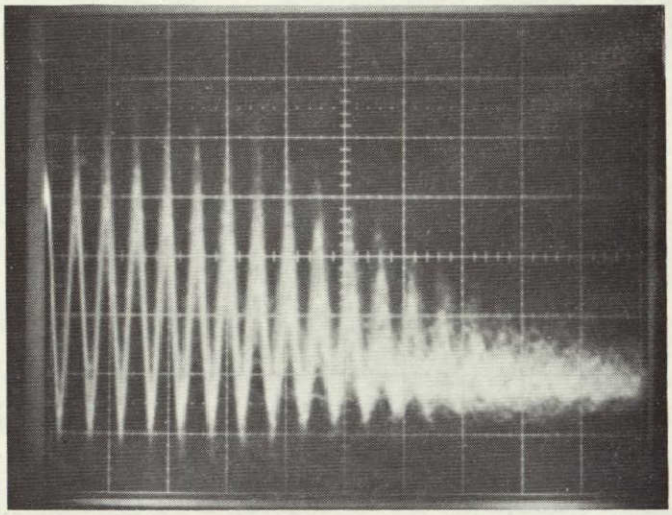

$\vec{u}$ - Component LDA Signal

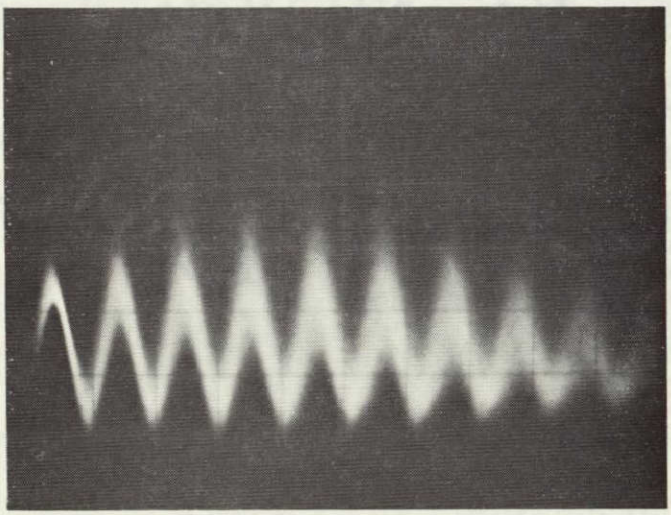

$\overrightarrow{(u + v)}$ - Component LDA Signal

Figure 13. Laser-Doppler anemometer signals at the outer edge of a turbulent boundary layer, $M_\infty = 2.2$, $Re_\theta = 40{,}000$.

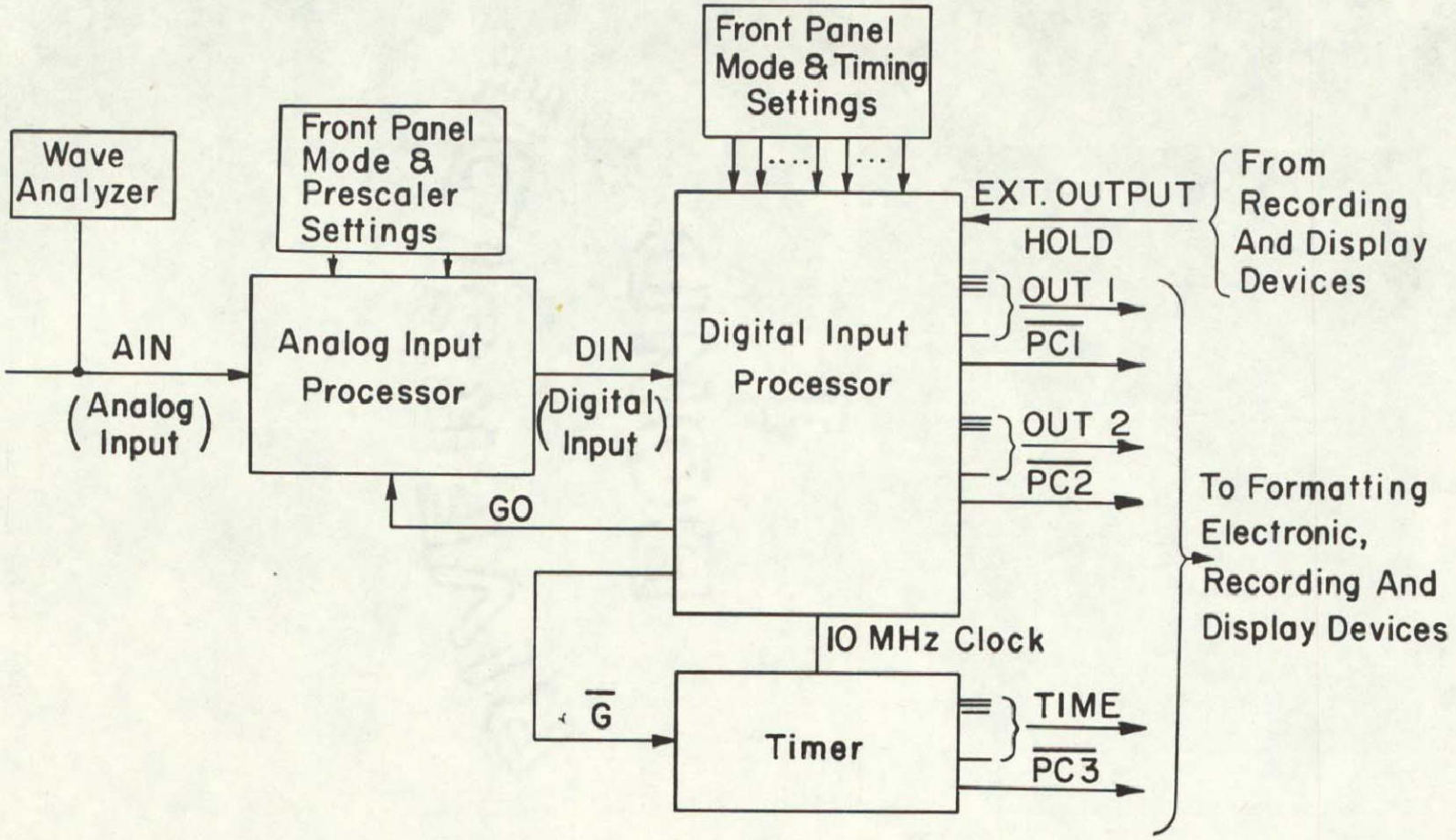

Figure 14. LDV processor block diagram.

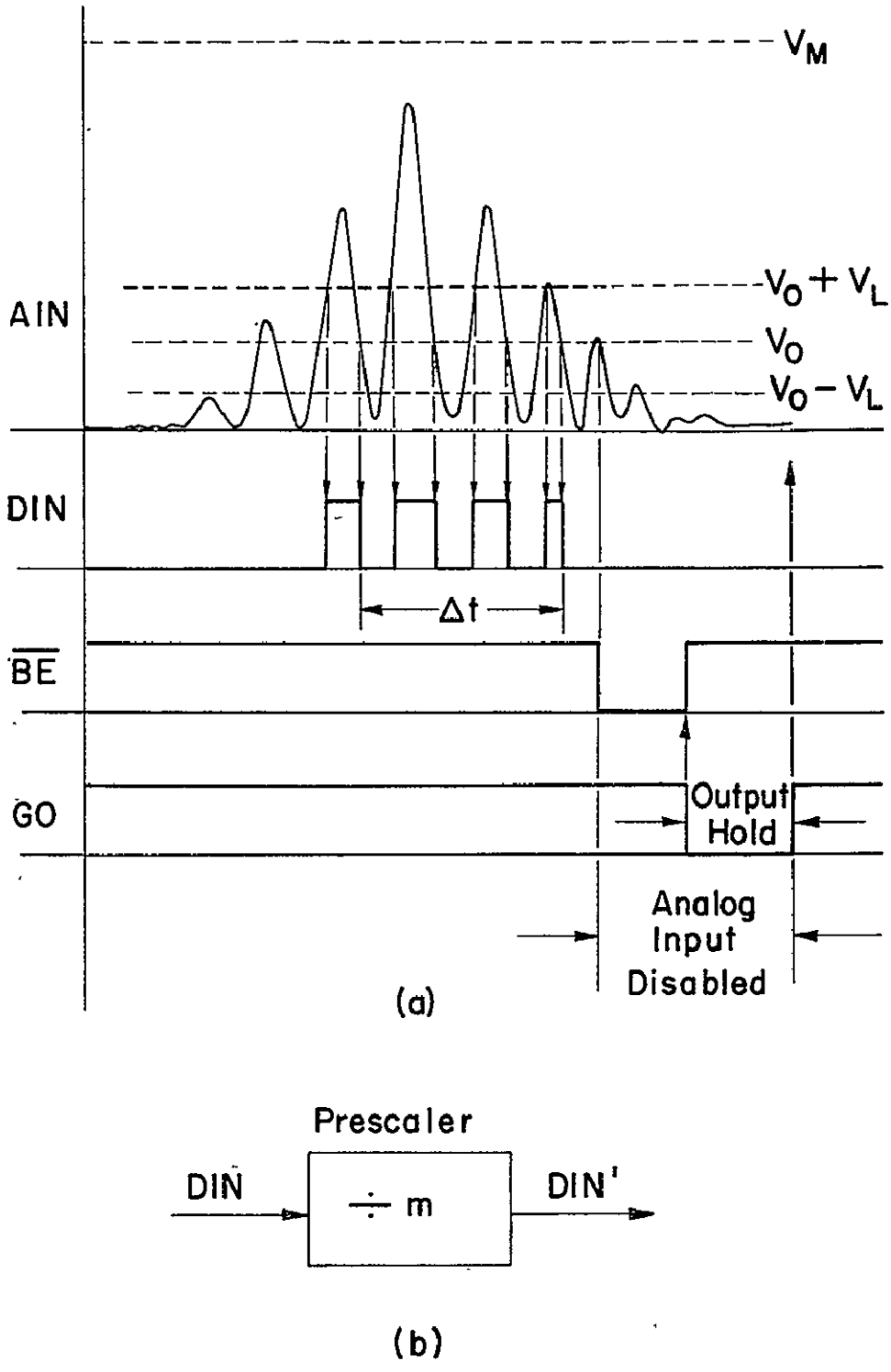

Figure 15. The analog processing technique.

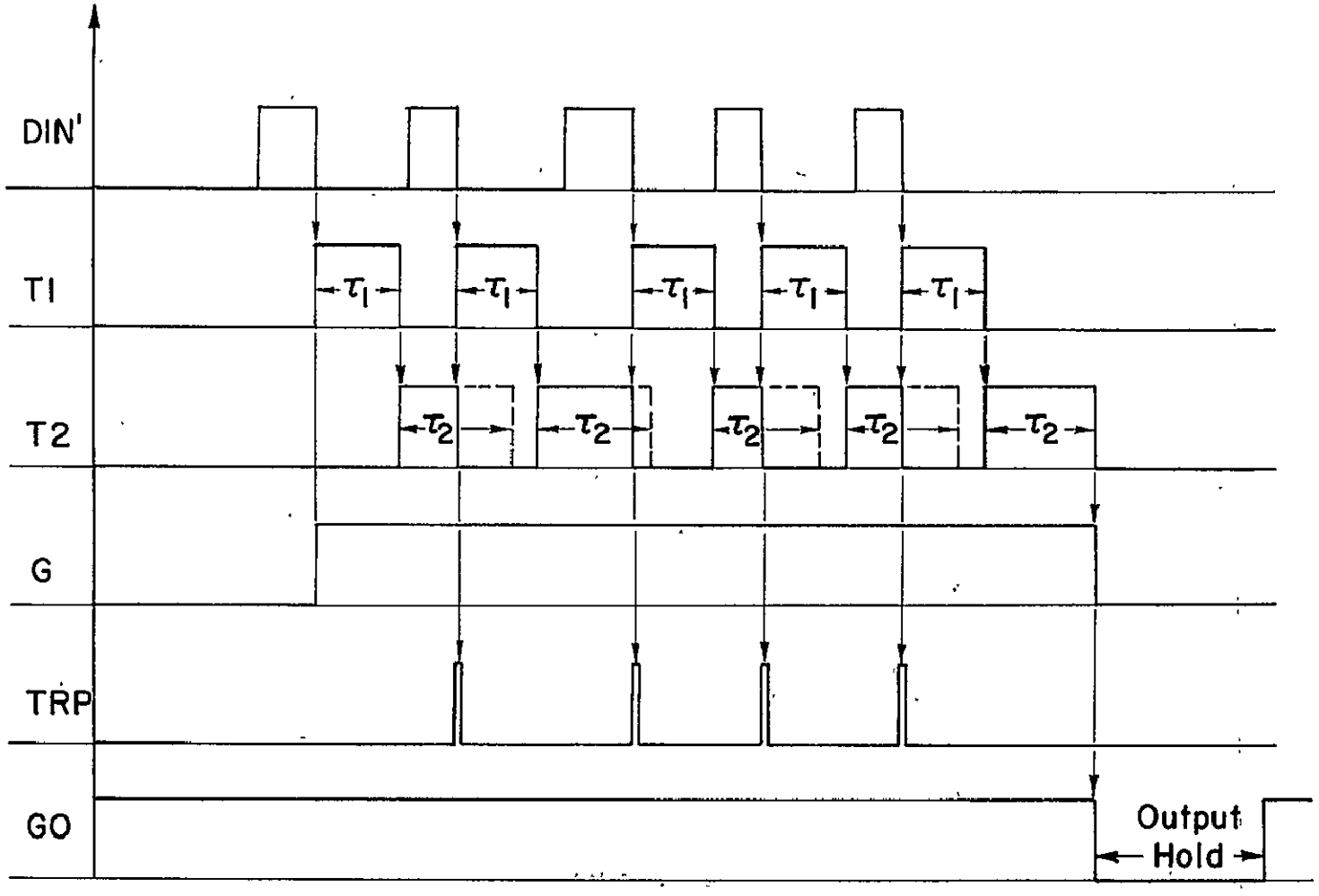

Figure 16. The logic associated with the digital input processor.

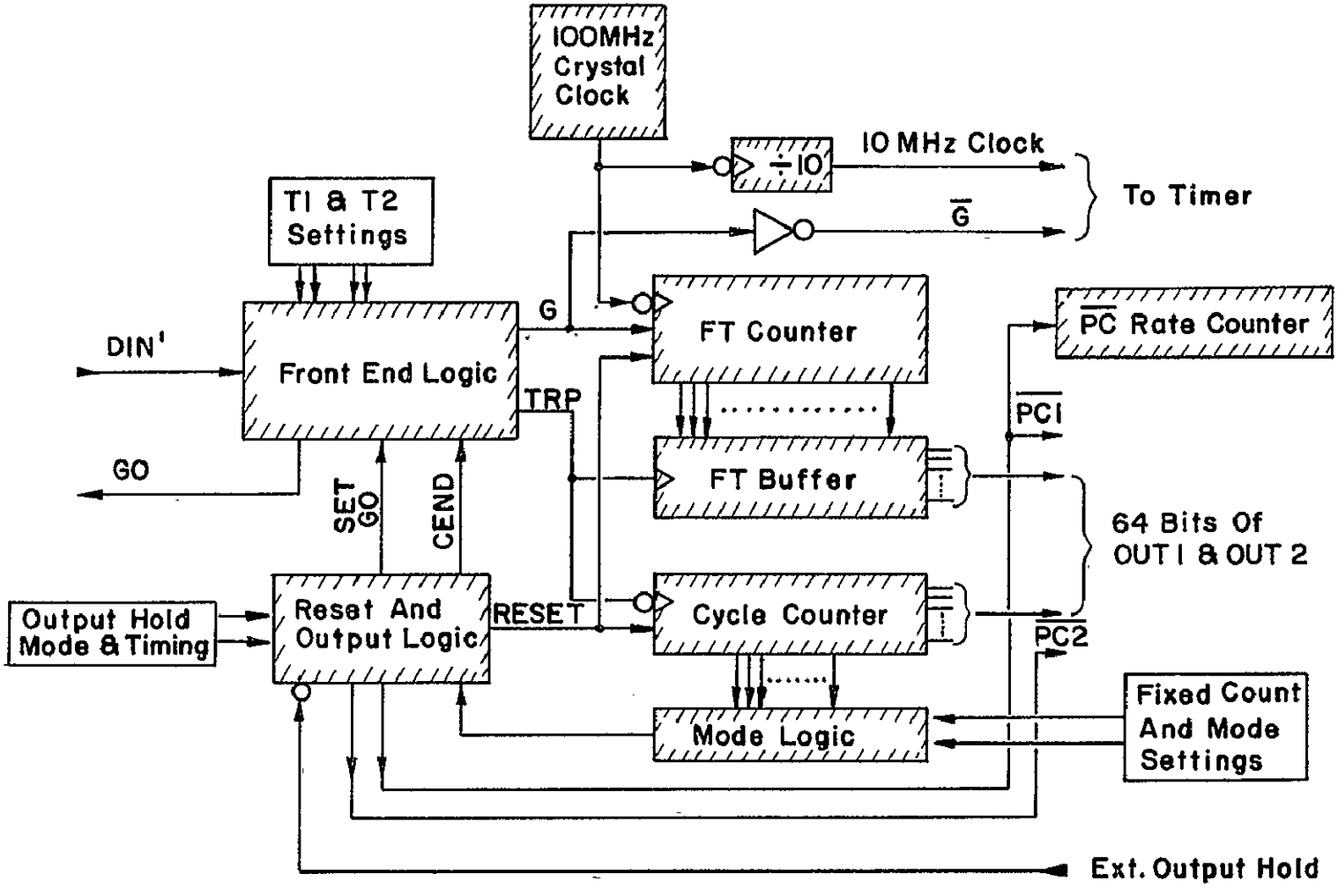

Figure 17. The digital input processor.

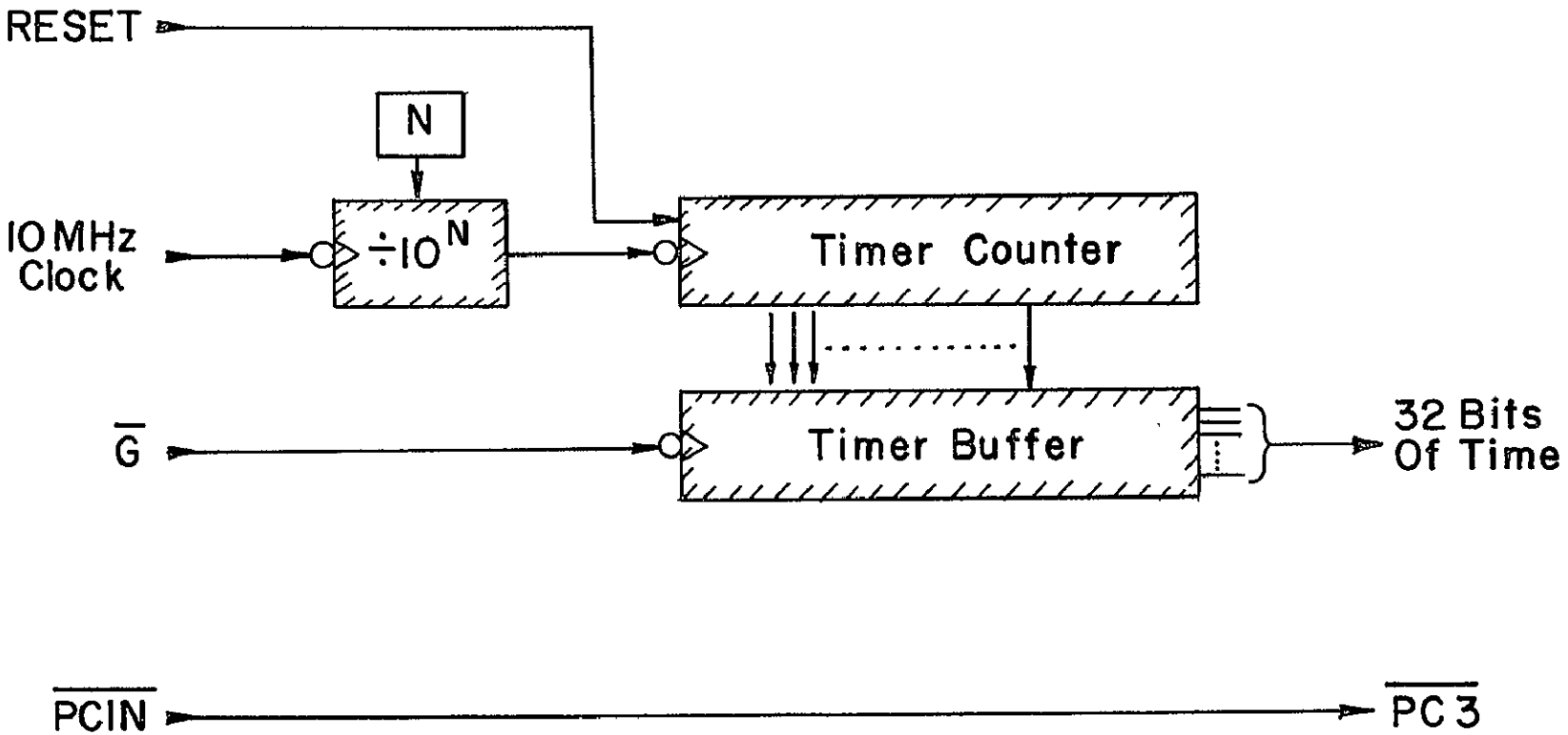

Figure 18. The timing circuit.

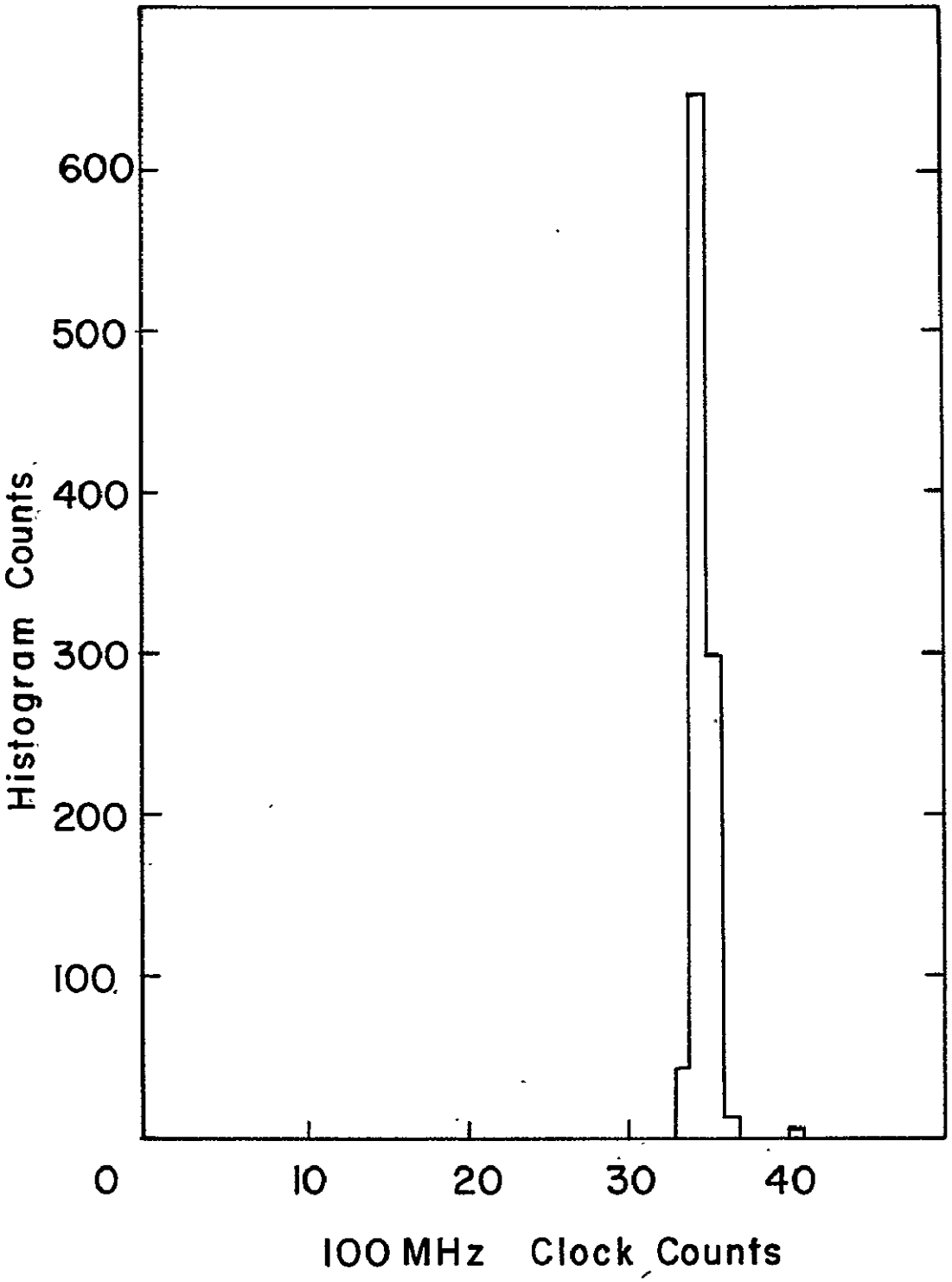

Figure 19. A typical histogram from the free-stream flow at M ≈ 2.2.

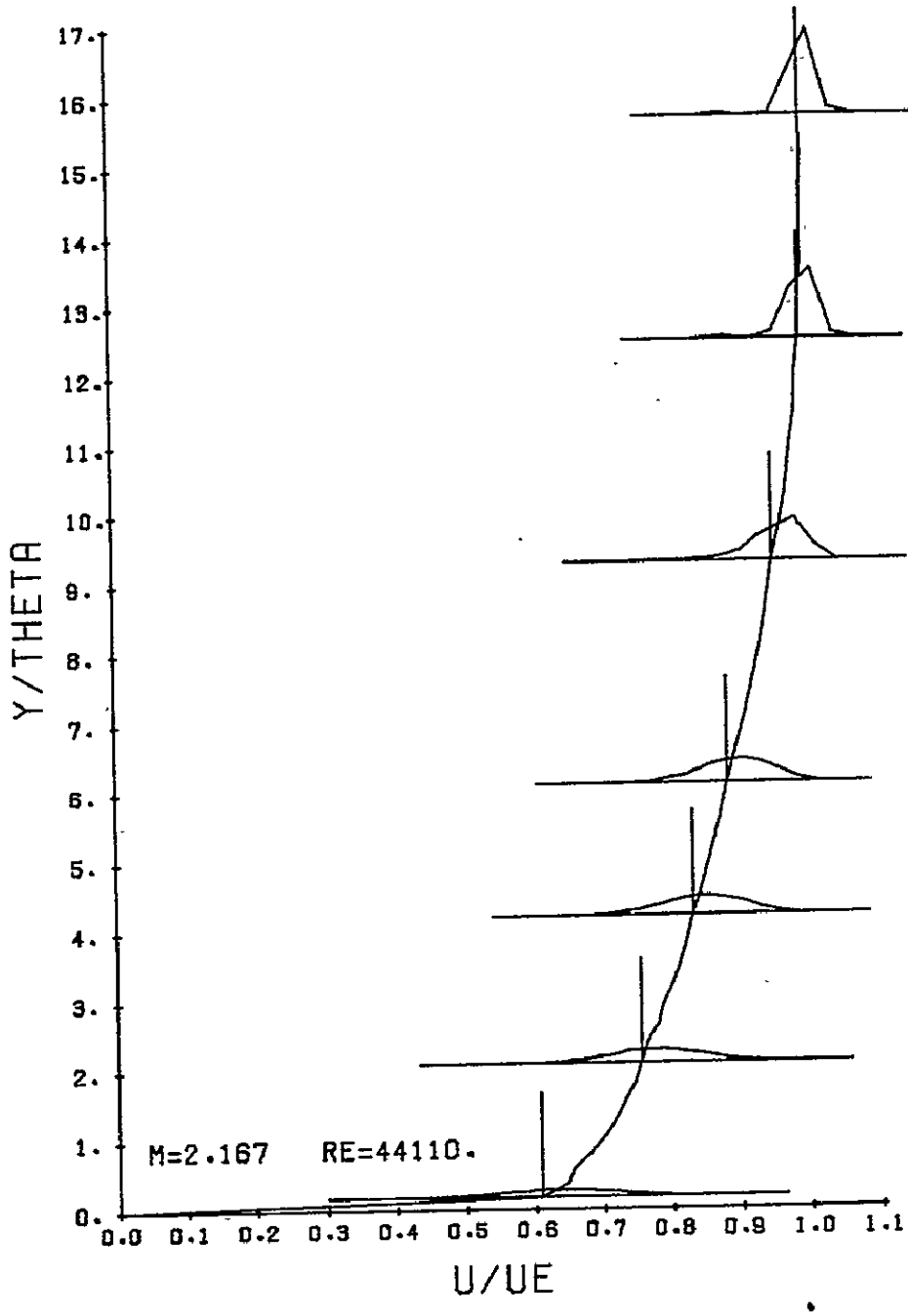

Figure 20. Representative histograms from the high-speed boundary layer.

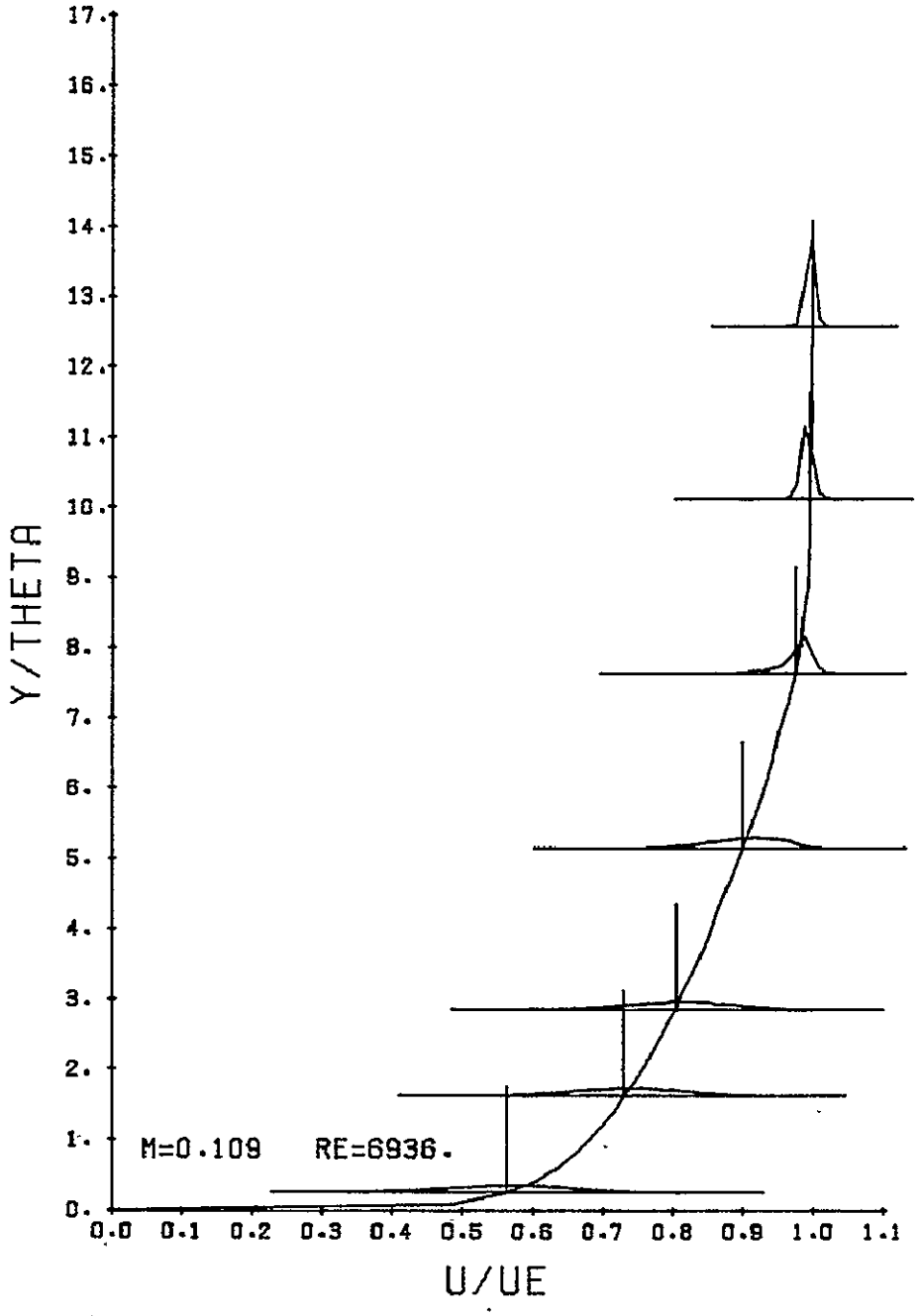

Figure 21. Representative histogram from the low-speed boundary layer.

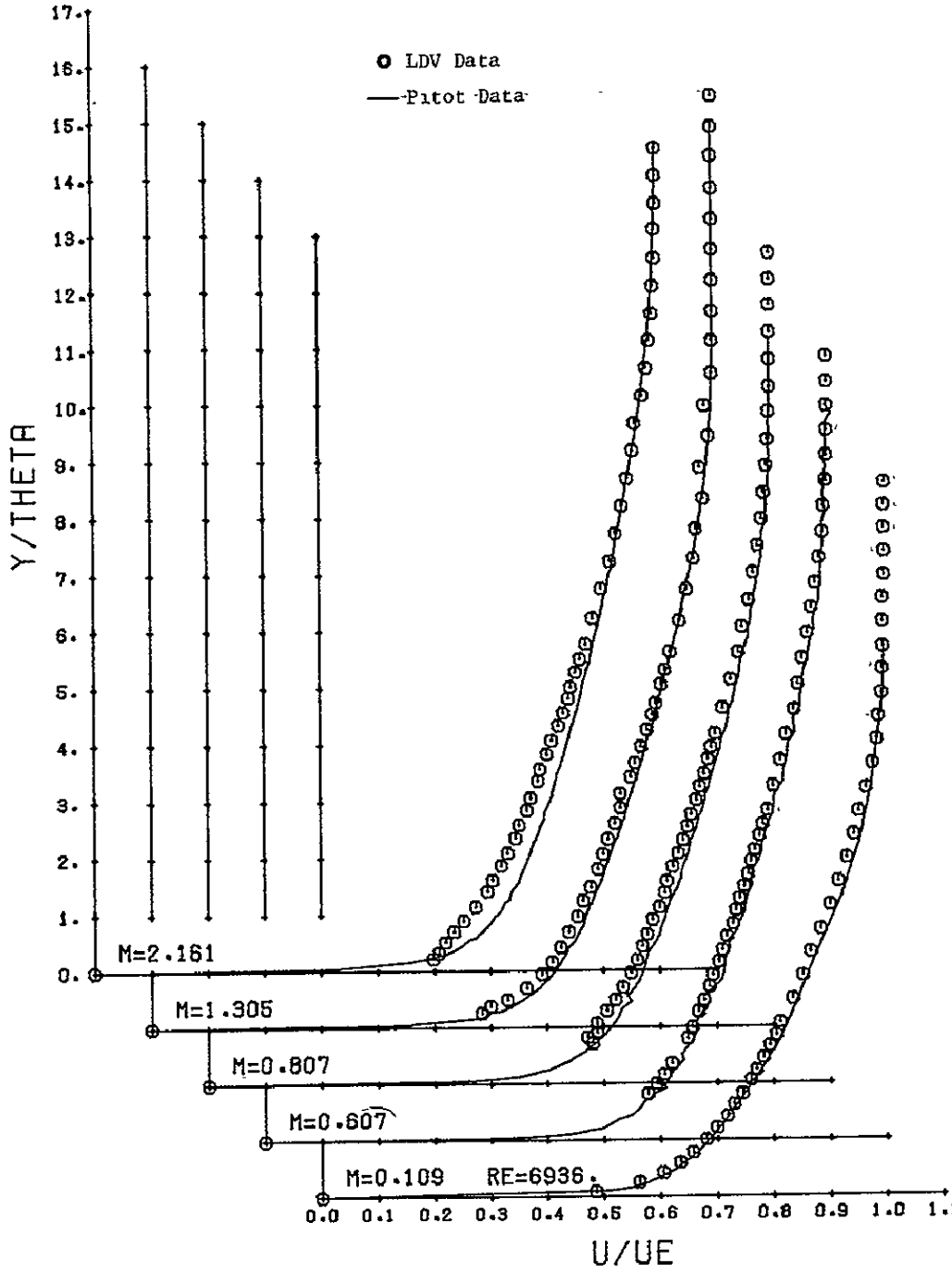

Figure 22.' Mean velocity profiles, Re_θ = 23,000.

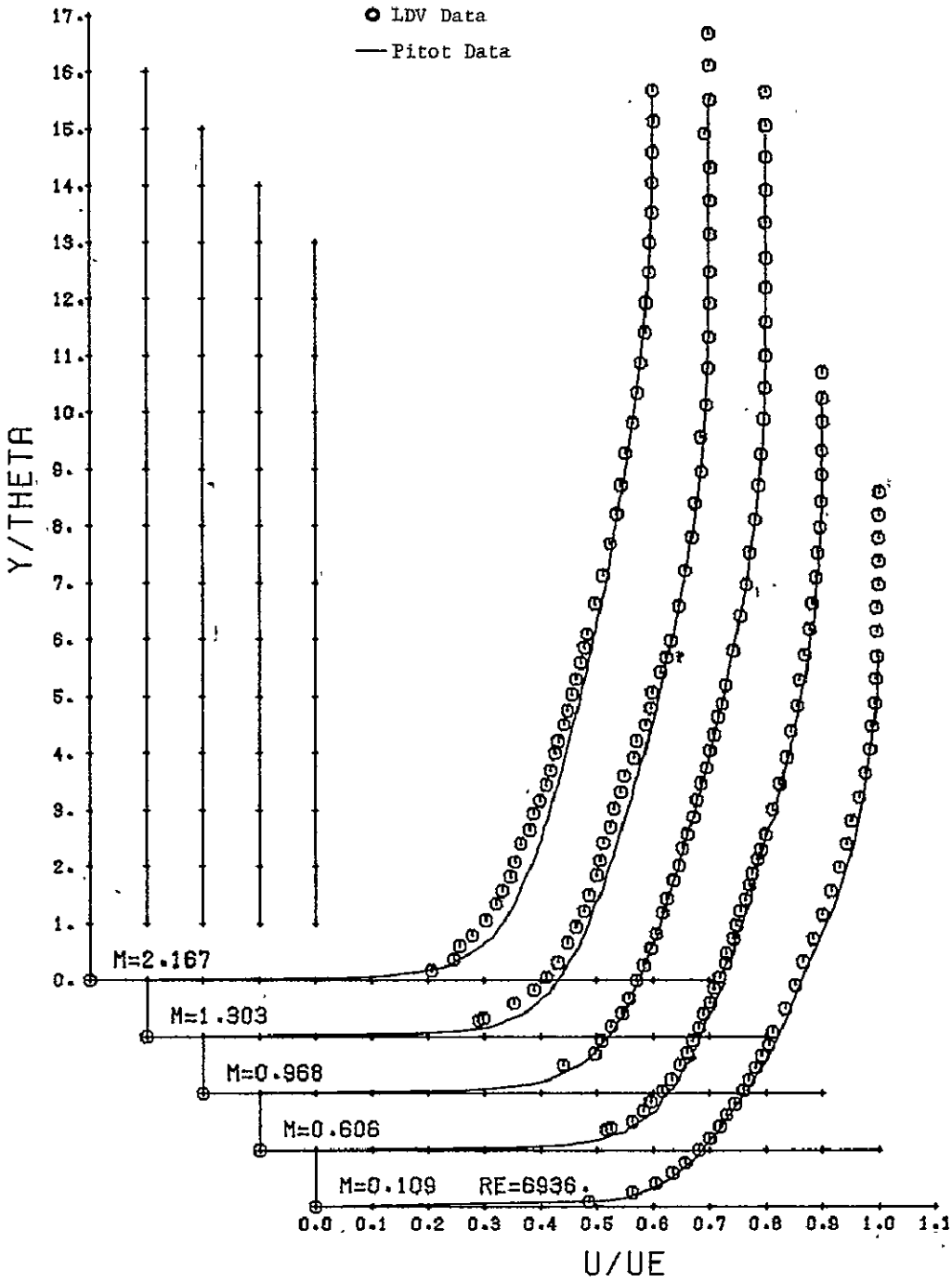

Figure 23. Mean velocity profiles, Re_θ = 40,000.

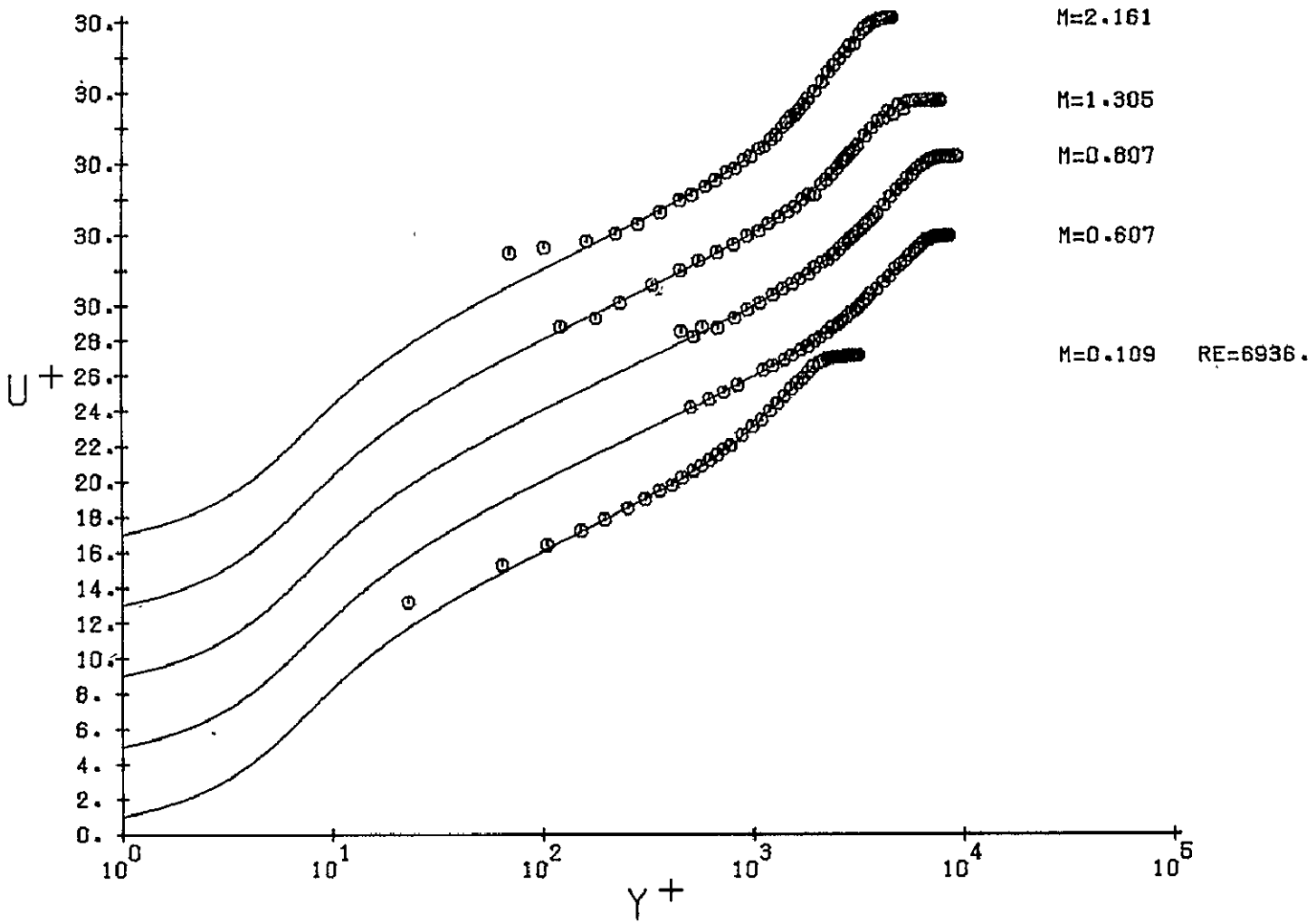

Figure 24. Mean velocity profiles with Van Driest scaling, Re_θ = 23,000.

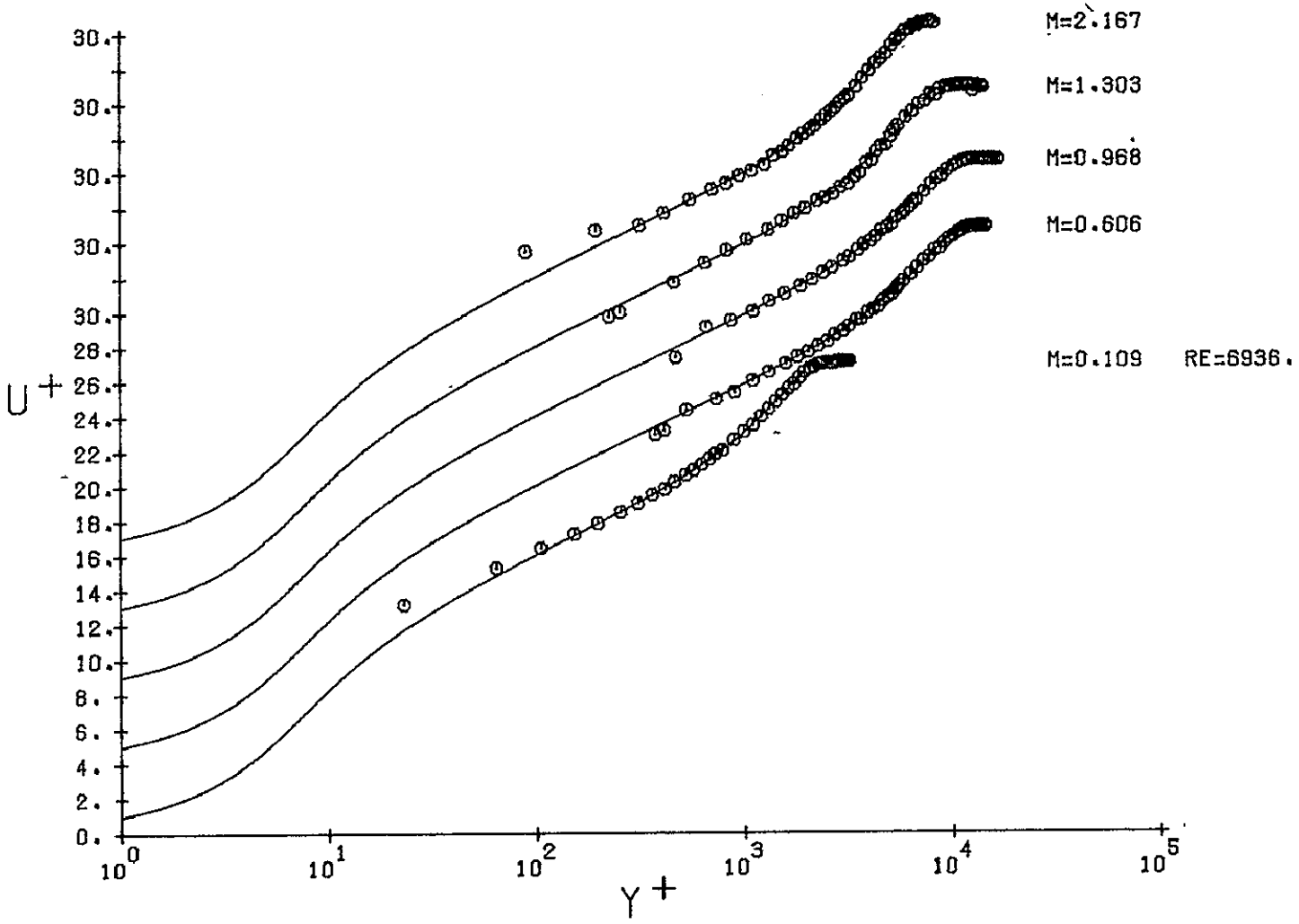

Figure 25. Mean velocity profiles with Van Driest scaling, Re_θ = 40,000.

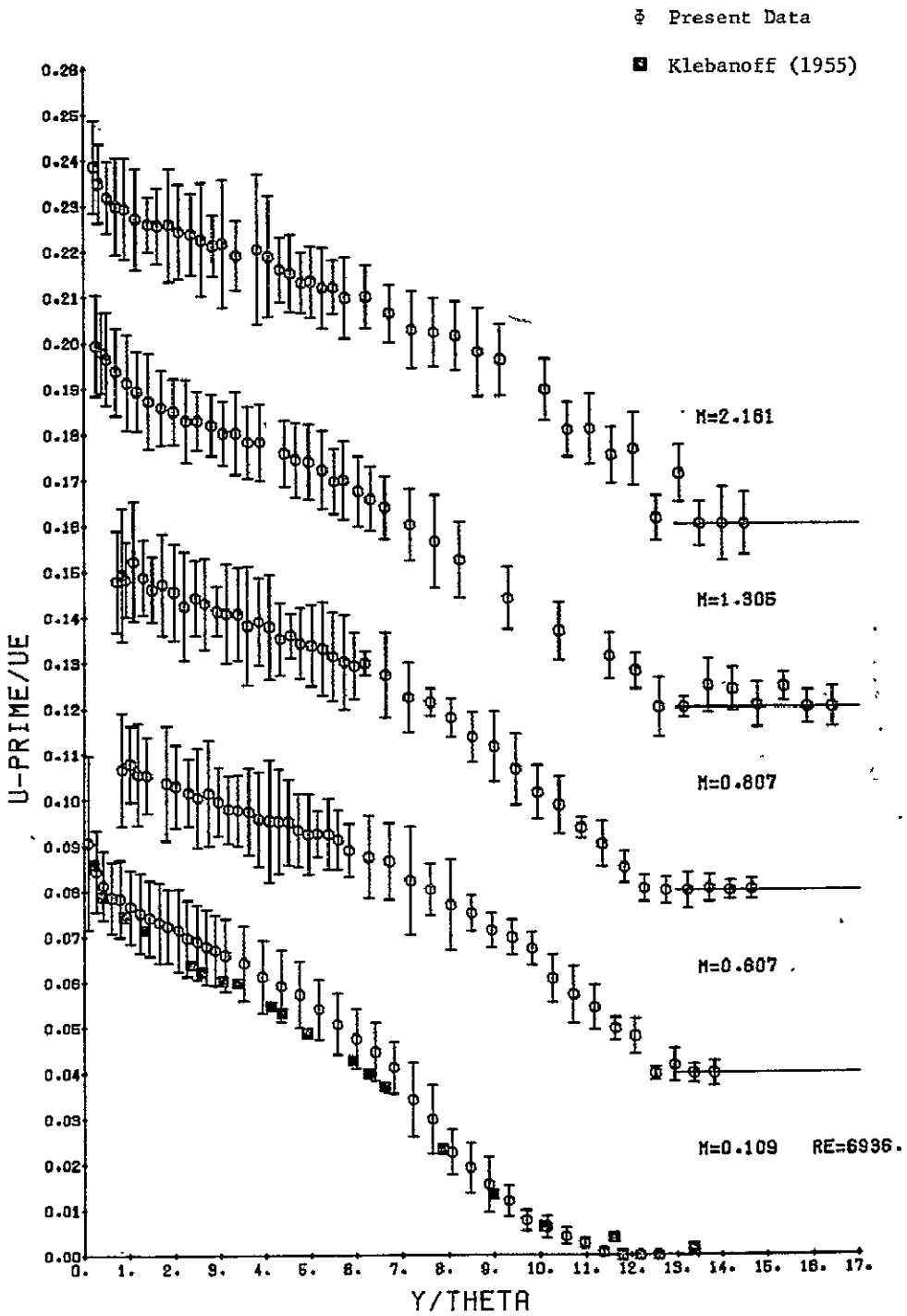

Figure 26. The streamwise velocity fluctuations, Re_θ = 23,000.

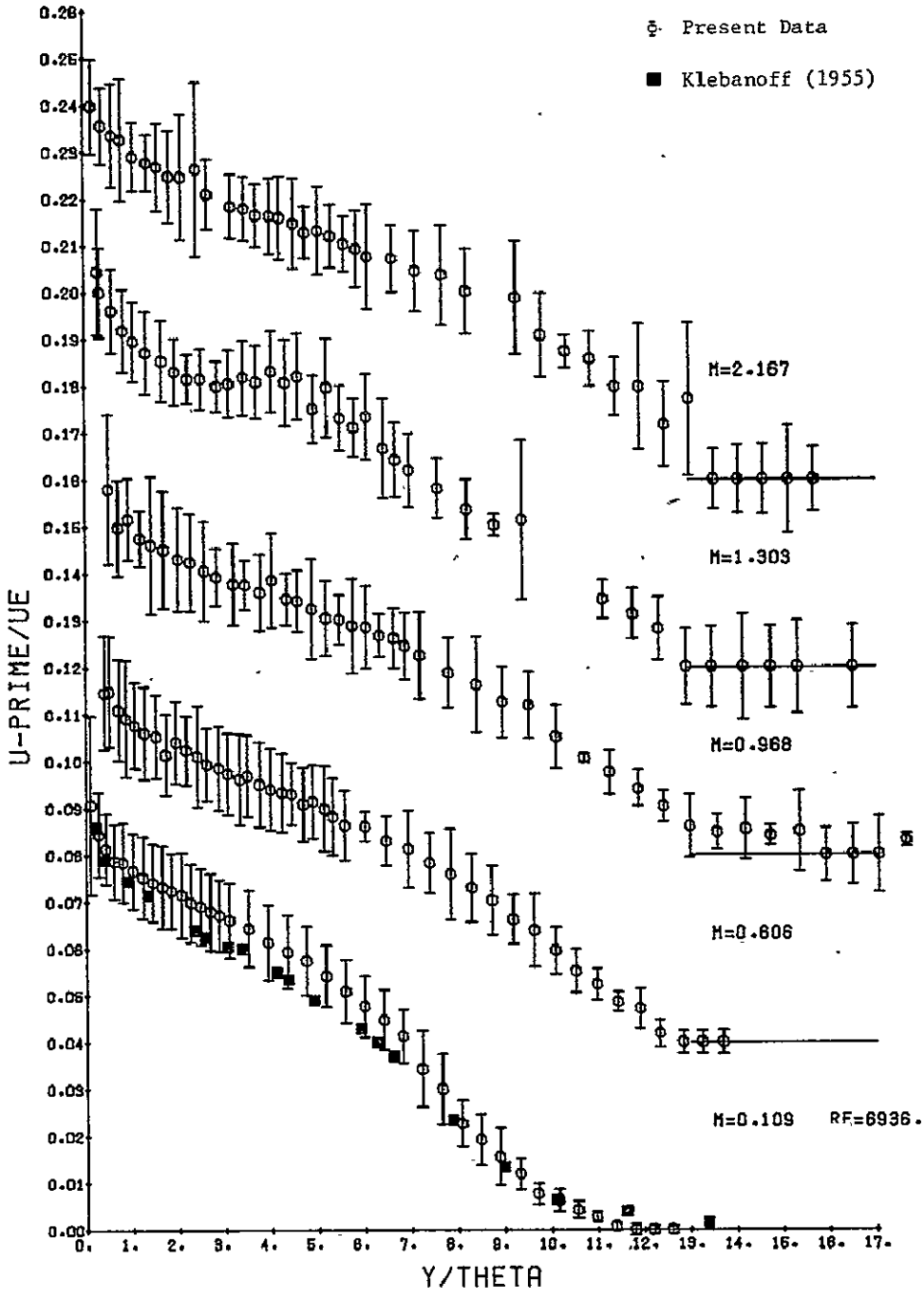

Figure 27. The streamwise velocity fluctuations, Re_θ = 40,000.

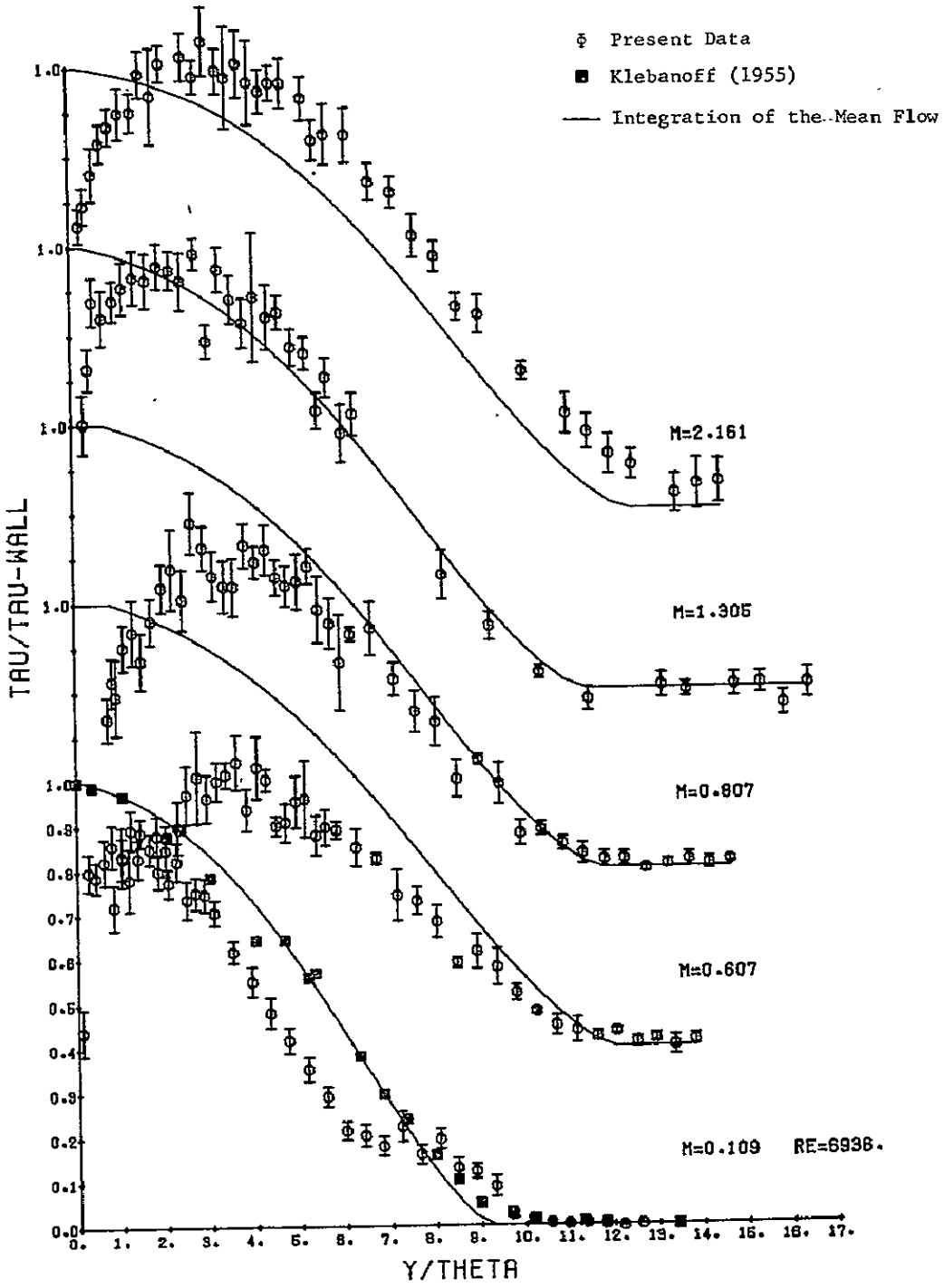

Figure 28. The distribution of Reynolds stress, Re_θ = 23,000.

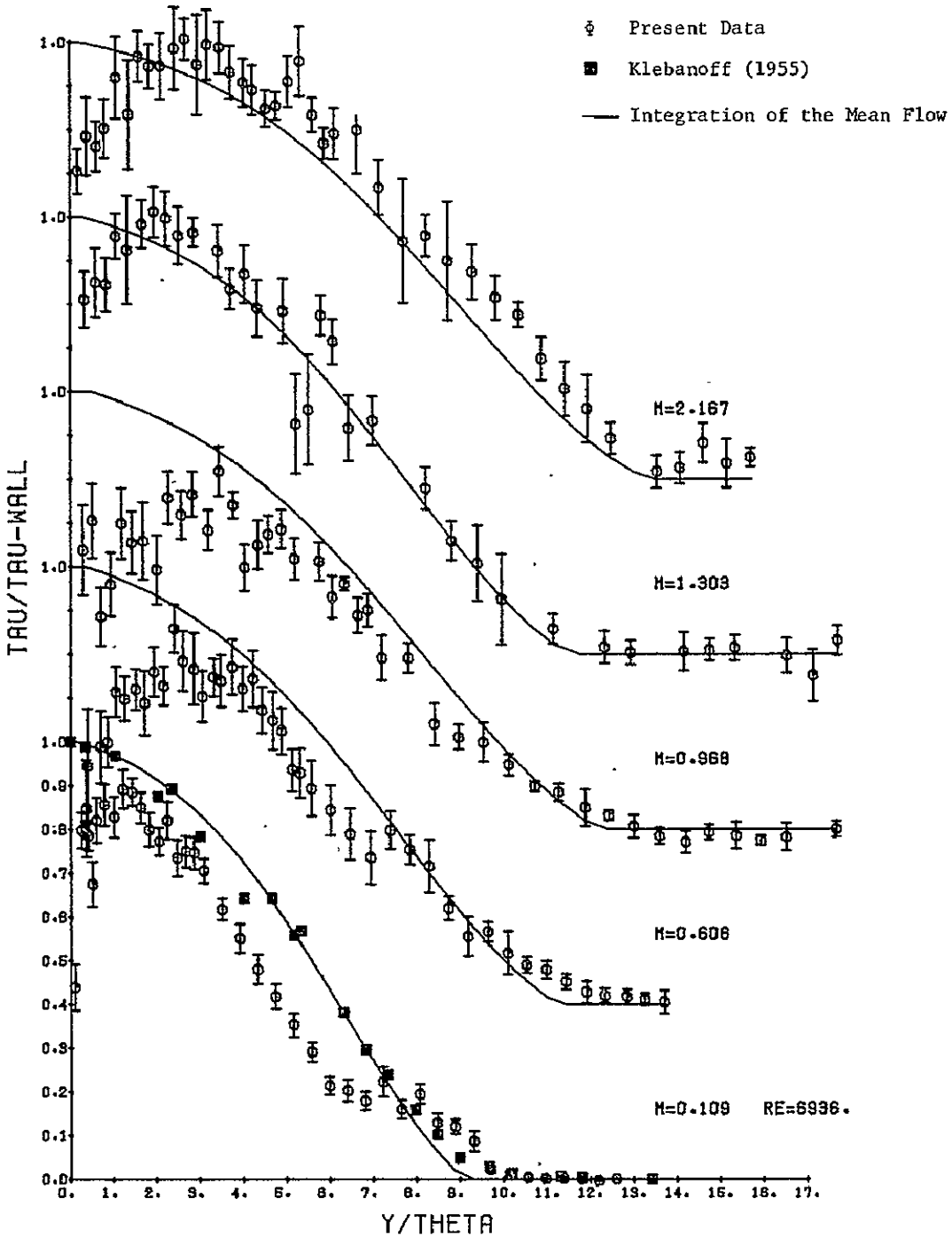

Figure 29. The distribution of Reynolds stress, Re_θ = 40,000.

Φ LDV Data

Integration of the Mean Flow

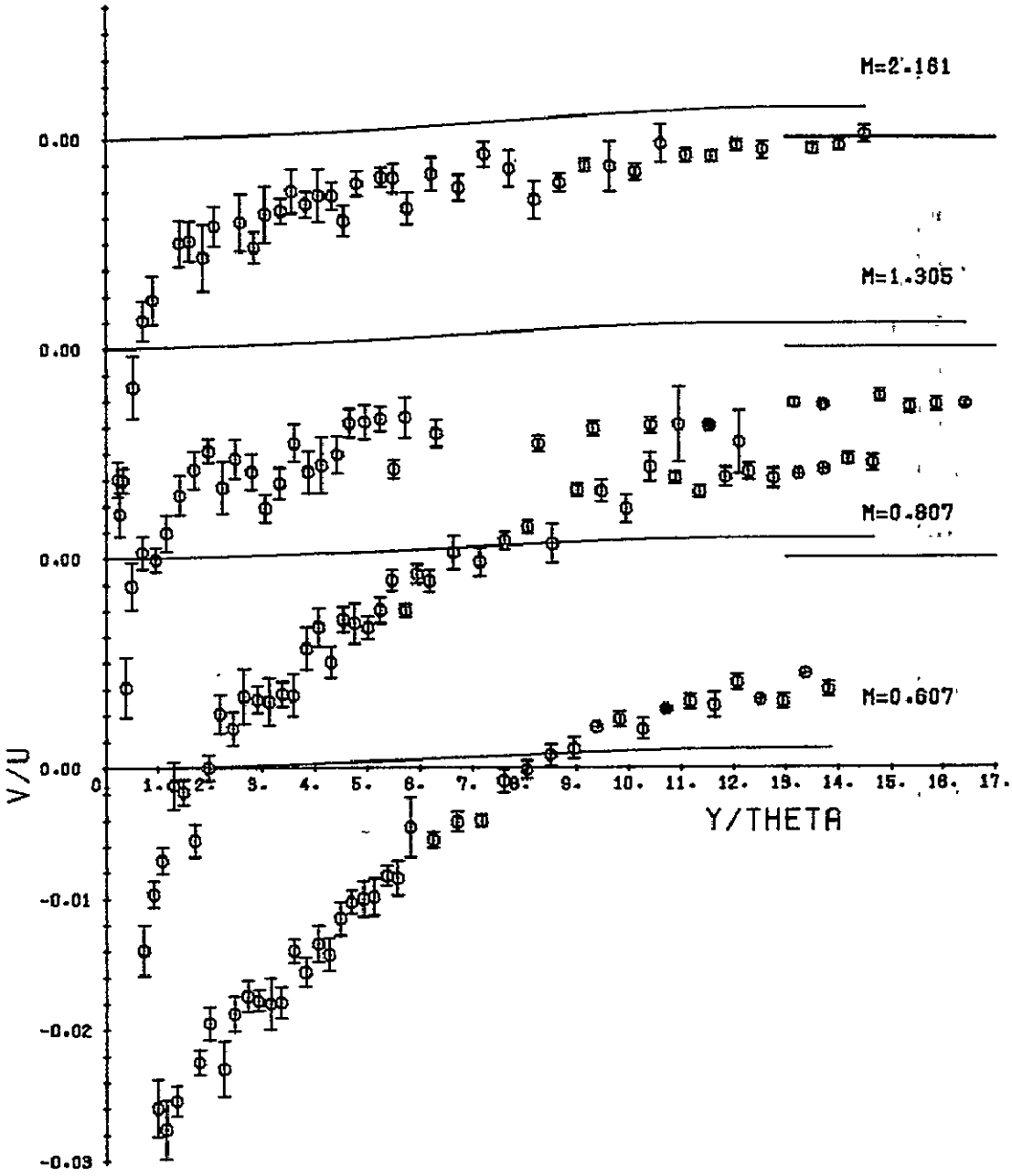

Figure 30. The distribution of normal velocity, Re_θ = 23,000.

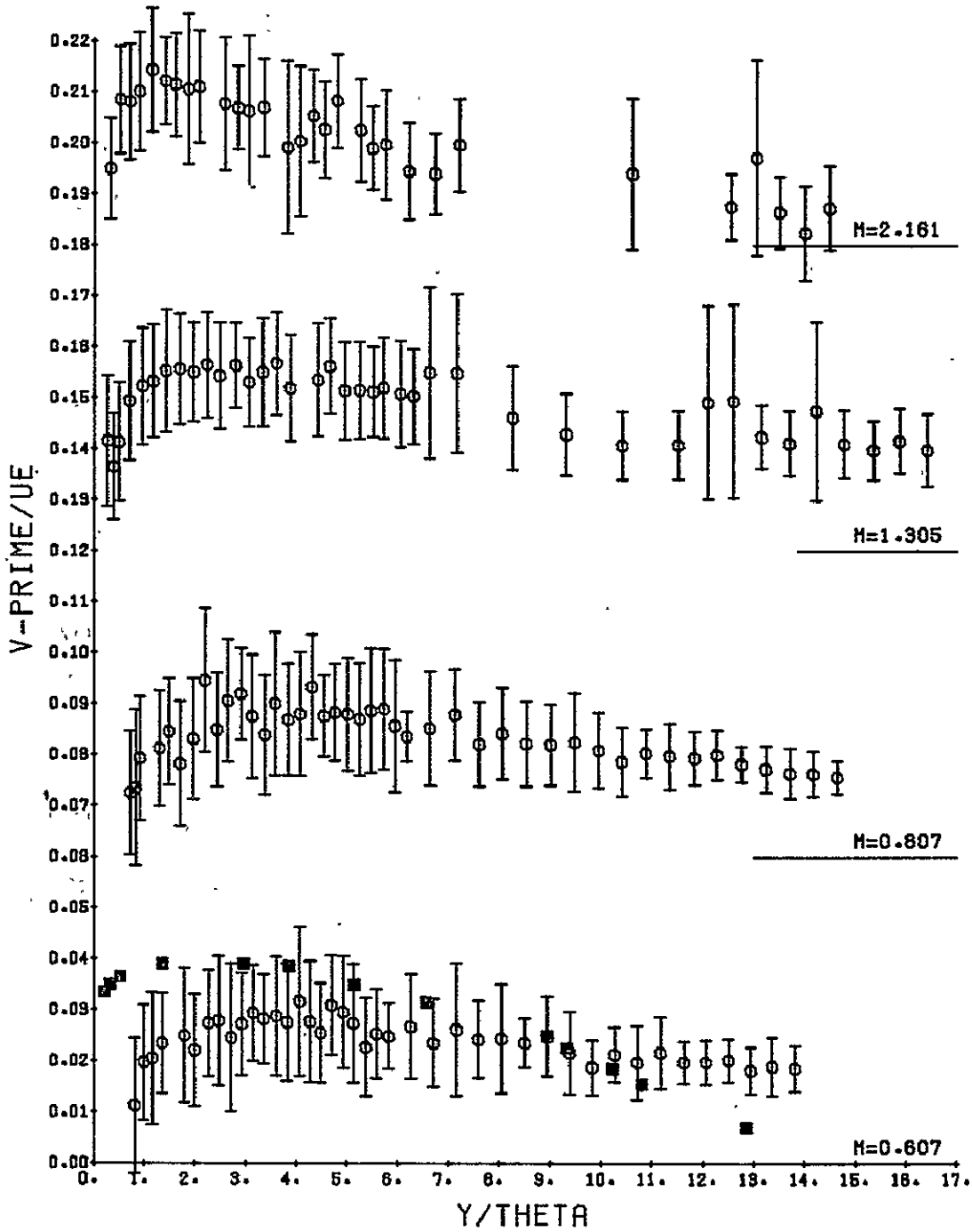

Figure 31. The distribution of the normal-velocity fluctuations, Re_θ = 23,000.

Nomenclature

Symbol	Equation	Meaning
c	(22)	constant in wall law (5.0)
C_f	(84)	local friction coefficient
d_p	(7)	particle diameter
k_i		integer output of the flight time counter
n	(21)	particle number density
n_i		number of observations with velocity u_i
Re_θ		Reynolds number based on θ
s	(2)	fringe spacing
u, v		streamwise and normal velocity components
u_i	(29)	velocity component in i^{th} direction
u_τ	(18)	friction velocity
$u_\perp$	(1)	velocity component normal to the fringe plane
$u_{/\!/}$		velocity component parallel to the fringe plane
x, y		streamwise and normal coordinates
α, β, γ, ϕ	Figure 12	angles defined by the beam planes
$\beta(u)$	(49)	bias function
δ	(26)	boundary-layer thickness
θ	(77)	boundary-layer momentum thickness
θ_i	Figure 12	beam separation angles
$\varkappa$	(22)	Kármán constant (0.41)
λ		laser wave length (0.5145 μm)
μ		viscosity
ν		kinematic viscosity

Nomenclature (Cont.)

Symbol	Equation	Meaning
ν_D	(1)	Doppler frequency
Π	(22)	strength of the wake component
τ_c	(5)	processor clock period
τ_p	(8)	particle response time
τ_w		shear stress at the wall

Subscripts

$( )_e$	edge or external value
$( )_f$	pertaining to the fluid
$( )_p$	pertaining to the particles
$( )_w$	wall value
$( )'$	rms fluctuations

Superscripts

$( )^+$	value made dimensionless with u_τ, ν_w